JOURNAL OF GEOPHYSICAL RESEARCH, VOL. 100, NO. C7, PAGES 13,681–13,698, JULY 15, 1995

Polarimetric signatures of sea ice
2. Experimental observations

S. V. Nghiem, R. Kwok, S. H. Yueh, and M. R. Drinkwater
Jet Propulsion Laboratory, California Institute of Technology, Pasadena

Abstract. Experimental observations of polarimetric signatures are presented for sea ice in the Beaufort Sea under cold winter conditions and interpreted with the composite model developed in Part 1. Polarimetric data were acquired in March 1988 with the Jet Propulsion Laboratory multifrequency airborne synthetic aperture radar (SAR) during the Beaufort Sea Flight Campaign. The experimental area was located near 75°N latitude and spanned 140°–145°W longitude. Selected sea ice scenes contain various ice types, including multiyear, thick first-year, and thin lead ice. Additionally, the *C* band SAR on the first European Remote Sensing Satellite provides supplementary backscattering data of winter Beaufort Sea ice for small incident angles (20°–26°) at vertical polarization. Sea ice characterization and environmental data used in the model were collected at the Applied Physics Laboratory drifting ice station to the northeast of Prudhoe Bay; additional data from field and laboratory experiments are also utilized in this analysis. The model relates sea ice polarimetric backscattering signatures to physical, structural, and electromagnetic properties of sea ice. Scattering mechanisms contributing to sea ice signatures are explained, and sensitivities of polarimetric signatures to sea ice characterization parameters are studied.

1. Introduction

Polarimetric signatures of sea ice need to be related to sea ice characterization parameters to infer relevant geophysical information from remote sensing data. A composite model for sea ice polarimetric scattering has been developed and presented in Part 1 [*Nghiem et al.*, this issue] to relate sea ice polarimetric signatures to physical, structural, and electromagnetic properties and processes in sea ice.

The objective of this paper is to connect measured polarimetric backscattering signatures to observed sea ice characteristics through the use of the sea ice model. Calibrated polarimetric data obtained over Beaufort Sea ice are presented and interpreted with the theoretical model for multiyear ice, first-year ice, and thin lead ice. During the Beaufort Sea Flight Campaign in March 1988, voluminous polarimetric data sets of sea ice were acquired at microwave frequencies by the Jet Propulsion Laboratory (JPL) synthetic aperture radar (SAR) over many locations in the Beaufort Sea containing various ice types. For the range of 20°–26° incident angles, the *C* band (5.3 GHz) SAR on the first European Remote Sensing Satellite (ERS 1) supplements vertical polarization data of winter sea ice in the Beaufort Sea [*Kwok and Cunningham*, 1994]. Sea ice characterization data and environmental conditions were recorded by the Applied Physics Laboratory's ice station (APLIS) in the same area. Numerous measurements and observations of ice characteristics are also available from other field and laboratory experiments.

From the same set of sea ice characterization parameters, the model calculates wave propagation, attenuation, and polarimetric scattering. The model includes volume scattering from ellipsoidal brine inclusions and spheroidal air bubbles with thermodynamic phase distribution of sea ice constituents. Effective anisotropy in sea ice is considered due to the structure of the ordinary ice polymorph in columnar ice. Layer thickness distribution, snow with randomly oriented spheroidal ice grains, brine skim and slush covers, and multiple wave interactions in anisotropic layered media are modeled. Rough interfaces with wave attenuation and differential phase delay and effects of hummocks on sea ice polarimetric signatures are accounted for.

Data for both polarimetric signatures and sea ice characterization are utilized in the model to analyze contributions from different scattering mechanisms, to explain trends observed in sea ice signatures, and to provide physical insights into the process of electromagnetic wave interactions in sea ice. An understanding of sea ice signatures and their relationship with sea ice characteristics will facilitate global ice monitoring and retrievals of geophysical parameters from sea ice remote sensing data.

Copyright 1995 by the American Geophysical Union.

Paper number 95JC00938.
0148-0227/95/95JC-00938$05.00

2. Beaufort Sea Flight Campaign

2.1. The Campaign

During March 1988, a series of NASA DC 8 missions were conducted over Arctic sea ice. This Beaufort Sea Flight Campaign (BSFC) was a part of the Defense Meteorological Satellite Program (DMSP) special sensor microwave/imager (SSM/I) validation experiment [*Cavalieri et al.*, 1991]. Over the experimental region in the Beaufort Sea, there were a number of sources of concurrent satellite (SSM/I, NOAA 9 and 10, and Landsat 4 and 5) and airborne data acquisitions, and characterization measurements of various ice types.

The DC 8 aircraft was equipped with the JPL multifrequency polarimetric SAR and the NASA Goddard Space Flight Center airborne multichannel microwave radiometer

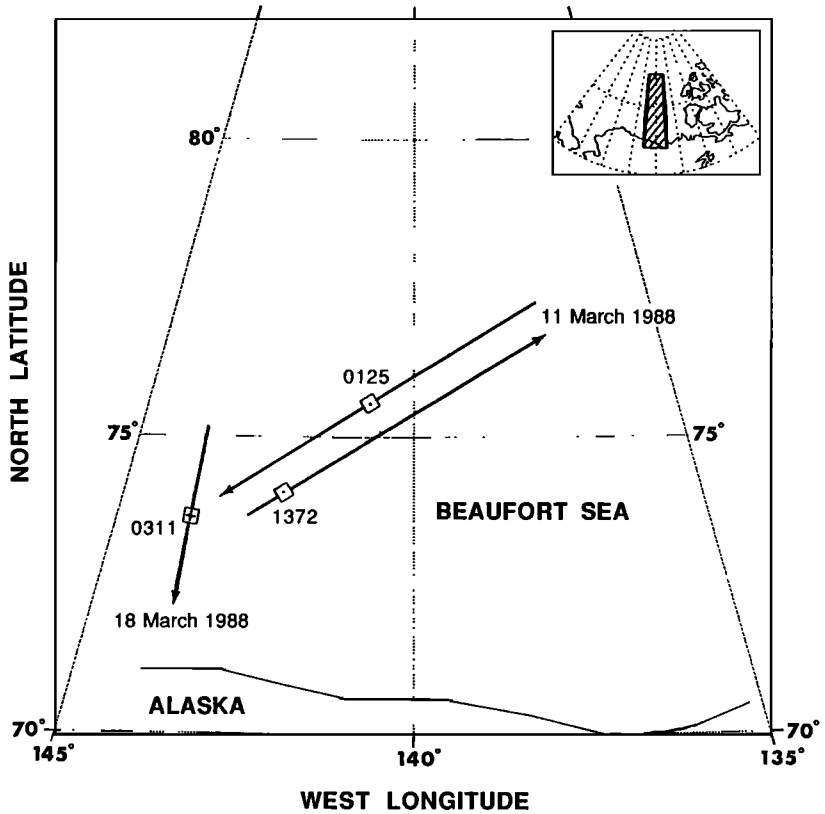

Figure 1. Map of sea ice scenes in the Beaufort Sea: scene 0311 contains the Applied Physics Laboratory ice station, scene 1372 is on the outbound, and scene 0125 is on the inbound flight legs.

(AMMR) [*Drinkwater et al.*, 1991a]. These two instruments collected simultaneous and spatially coincident data. The flights were synchronized with SSM/I satellite radiometric imaging of the same regions. Weather and ice characterization data were collected at a drifting ice station throughout the campaign.

2.2. Sea Ice Scenes

The locations of three representative sea ice scenes, which will be used for the analysis in this paper, are shown on the map in Figure 1. On March 11, 1988, polarimetric SAR scenes of sea ice in the Beaufort Sea were acquired on a flight between the coast of Alaska and the northern tip of Ellesmere Island. Data were collected continuously along the outbound flight on a compass heading of around 25° relative to magnetic north. Scene 1372, acquired during the outbound flight, is selected, since it contains thin ice in new leads together with first-year and multiyear ice. On the inbound return leg, data were also collected, and scene 0125, including more data on first-year and multiyear ice, is considered.

On March 18, 1988, the JPL SAR was flown over the Applied Physics Laboratory's drifting ice station. A sea ice scene acquired over the ice station is identified as scene 0311 and represented by a cross in Figure 1. The ice station was set at the edge of a multiyear ice floe, adjacent to a frozen lead containing thick first-year sea ice. Ice characterization measurements obtained from the station will be used in the analysis of JPL SAR data.

The three scenes, obtained during three different flight headings, are located near 75°N latitude and spanned a distance within 140°–145°W longitude. Sea ice images of the scenes at L band are shown in Figure 2. The JPL SAR operates at three different center frequencies: 5.3 GHz in C band, 1.25 GHz in L band, and 0.44 GHz in P band. Fully calibrated polarimetric data are not yet available at P band; therefore all results in this paper are from C and L band radars.

2.3. Polarimetric Data

The radar transmits linear horizontal polarization and measures magnitudes and phases of both vertically and horizontally polarized returns. Vertical polarization is then transmitted, and the radar receives both horizontal and vertical waves in the backscattering direction. From these polarimetric measurements, all elements in the complex scattering matrix are obtained and recorded digitally. Scattering matrix data are subsequently processed, with proper consideration of polarimetric calibration, into Stokes matrix and covariance matrix outputs, which contain information regarding polarimetric backscattering signatures of sea ice.

A covariance matrix is composed of polarimetric scattering coefficients, which are correlations between all possible combinations of elements in the scattering matrix. A Stokes or Mueller matrix, which relates the scattered to the incident Stokes vector, is derived from the polarimetric scattering coefficients. Polarimetric calibration can be done with point targets such as corner reflectors deployed in scenes [*Yueh et al.*, 1990]. Here, polarimetric data are calibrated with another method using the reciprocity and symmetry character-

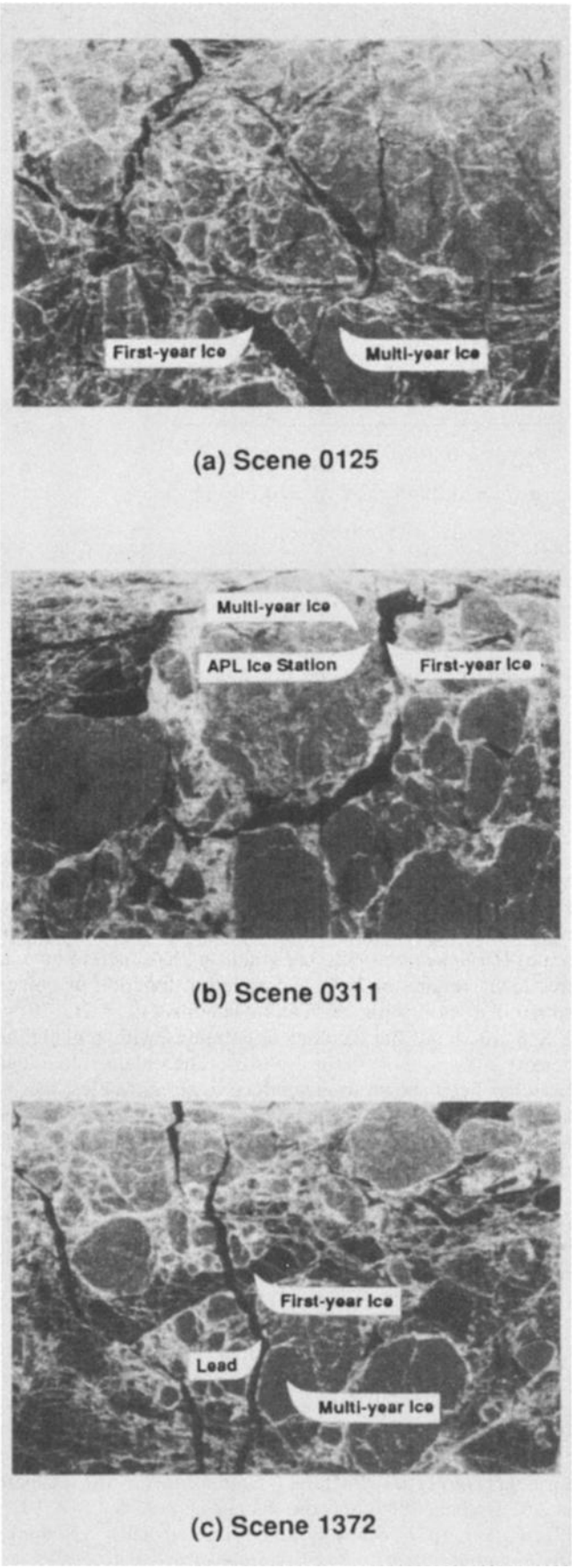

Figure 2. Images of sea ice scenes (a) 0125, (b) 0311, and (c) 1372.

istics of the natural scattering configuration without in-scene deployment of man-made targets [*Yueh et al.*, 1992, 1993]. In this paper, sea ice polarimetric data acquired over the Beaufort Sea are taken from six images for the three sea ice scenes at the *C* band and *L* band frequencies.

3. Sea Ice Characterization

3.1. Sea Ice Characteristics and Environmental Conditions

Weather and sea ice characterization data were collected continuously during March at the APLIS station located about 350 km northeast of Prudhoe Bay, Alaska. Meteorological and ice measurements were taken by *Wen et al.* [1989] and summarized here together with synoptic information from weather records.

Sea ice conditions in the vicinity of the scenes indicated in Figure 1 pertained to a zone extending northward from around 72.5°N and made up of a transition from a coastal first-year ice region to a heavy multiyear ice pack to the north. It is identified in the SSM/I and SAR images as having mixed first-year and multiyear ice types with multiyear ice fractions ranging from 35% to 70% and a total concentration of 100% [*Drinkwater et al.*, 1991a; *Cavalieri et al.*, 1991]. Air temperatures varied between −12°C and −18°C on March 11 and colder (below −25°C) during an earlier period in March.

The APLIS station is located in the upper part of scene 0311 in Figure 2b. Observations from the ice station helped identify ice types in scene 0311, which in turn, was used in the identification of ice types in other scenes. First-year ice in the vicinity of the ice station was 1.5–2.4 m thick and covered by a snow layer with an average depth of 15.0 cm. Multiyear ice was also covered by snow with a hummock surface. Floes of multiyear ice were typically surrounded by deformed first-year ice.

In general, multiyear ice appears brighter than first-year ice in the sea ice images; examples of the ice types are indicated in Figure 2 for the three scenes. Few new leads are evident in the vicinity of the images, and the total area of new ice formation was particularly small due to a lack of recent ice divergence. The only divergence occurring close to the period of SAR data collection was experienced on March 10, when high ice drift velocities were recorded. The ice station drift velocity also responded to a wind event during this period of divergence, with a peak drift speed of 32 cm s^{-1}. Sea ice scene 1372 on March 11 reveals images of new cracks and leads, as seen in Figure 2c, created by the divergent ice motion. Open leads rapidly frozen under the cold conditions became new thin ice formations.

3.2. Additional Characterization Data

Over several decades, many expeditions and experiments have been carried out to observe and measure sea ice properties and processes in the Beaufort Sea and other locations in polar oceans. To derive the empirical relationship between average salinity and ice thickness, *Cox and Weeks* [1974] assembled field data taken in the Beaufort, Bering, Labrador Seas and Viscount Melville Sound from 1955 to 1972. The presence of a thin, highly saline layer of slush on the surface of young sea ice has been reported [*Drinkwater and Crocker*, 1988]. During the Lead Experiment (LeadEx) [*LeadEx Group*, 1993] in the Beaufort Sea, *Perovich and Richter-Menge* [1994] observed a very high

salinity (100‰) in a surface skim on new lead ice. A detailed examination of a freezing lead was also made by *Gow et al.* [1990] during the drift phase of the Coordinated Eastern Arctic Experiment (CEAREX) [*CEAREX Drift Group*, 1990].

From the Beaufort Sea Ice 1 (BSI1) campaign, characterization data of snow cover on sea ice [*Drinkwater*, 1992] and surface roughness data are also available [*Carlström*, 1992; M. R. Drinkwater, unpublished data, 1990]. Profiles for hummock surfaces at air-snow and snow-ice interfaces have been measured over multiyear ice in the Beaufort Sea near the Arctic Ice Dynamics Joint Experiment (AIDJEX) camp [*Cox and Weeks*, 1974]. The hummock measurements were carried out during March–April, which is the same seasonal time as the BSFC. The location of the AIDJEX camp was further west of the APLIS and approximately at the latitude of the sea ice scenes acquired by the JPL SAR. More data of sea ice properties in the Beaufort Sea can be found in a report by *Meese* [1989]. Cold Regions Research and Engineering Laboratory Experiments (CRRELEX) also give additional useful information. In the following sections, polarimetric signatures of multiyear ice, first-year ice, and thin lead ice are examined with the composite model (presented in Part 1).

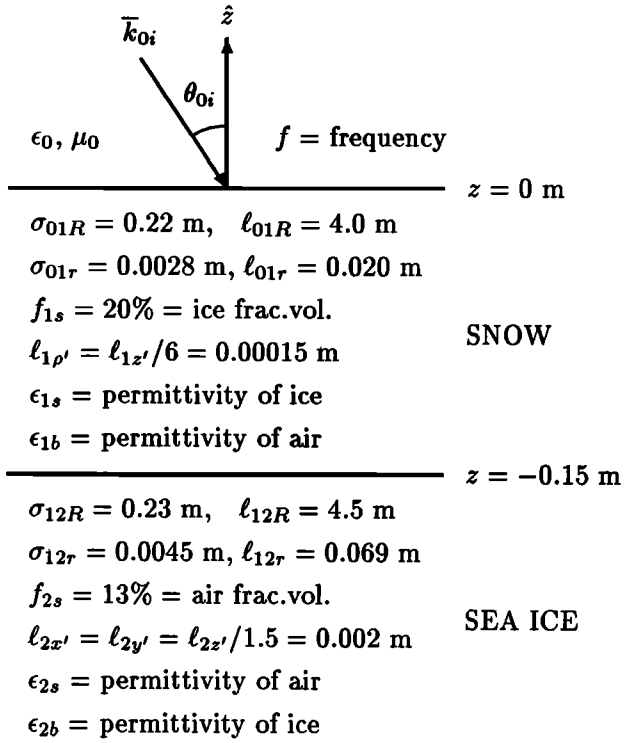

Figure 3. Physical parameters for multiyear sea ice.

4. Multiyear Sea Ice

4.1. Characterization Parameters

Multiyear sea ice in the Arctic is distinguished by a hummock surface (see section 2.5 in Part 1) due to differential melt, and by very low salinity due to flushing of surface meltwater during summer seasons [*Weeks and Ackley*, 1982]. In winter conditions, multiyear ice primarily contains ice and air bubbles with a minute volume in liquid phase as a result of cold temperature and near-zero salinity except near the boundary of ice and seawater. Multiyear ice is usually thick, and scattering at microwave frequencies is predominantly from the upper part of the ice layer.

From hummock profiles obtained near the AIDJEX camp [*Cox and Weeks*, 1974], correlation functions of hummock air-snow and snow-ice surfaces are found to agree well with Gaussian forms as shown in Figure 5 of Part 1 [*Nghiem et al.*, this issue], where exponential functions with the same correlation lengths are also plotted for comparison. For the hummock air-snow surface, height standard deviation is $\sigma_{01R} = 0.22$ m and correlation length is $\ell_{01R} = 4.0$ m, where subscript 01 denotes the interface between air (region 0) and snow (region 1). The hummock surface between snow and ice layers has a height standard deviation of $\sigma_{12R} = 0.23$ m and a correlation length of $\ell_{12R} = 4.5$ m. Note that hummock roughnesses of the air-snow and the snow-ice surfaces are very similar. Correlation between slopes of the two surfaces shows a correlation coefficient of 0.92, and the slopes can be fitted to each other linearly with a coefficient of 0.9 and almost no bias. This indicates that the two hummock surfaces are approximately in parallel, as depicted by the model for multiyear sea ice presented in Part 1.

Results from the BSI1 campaign provide typical small-scale roughness values with height standard deviation $\sigma_{01r} = 2.8 \times 10^{-3}$ m and correlation length $\ell_{01r} = 2.0 \times 10^{-2}$ m for the air-snow surface and $\sigma_{12r} = 4.5 \times 10^{-3}$ m and $\ell_{12r} = 6.9 \times 10^{-2}$ m for the snow-ice interface. Scattering contributions from the composition of hummock topography and small-scale roughnesses at the interfaces in multiyear ice are all calculated with the Kirchhoff approximation described in section 3.5 of Part 1.

Multiyear ice is usually covered under a layer of dry snow during winter. The average thickness of the snow layer is reported at the APLIS to be 0.15 m [*Wen et al.*, 1989]. Snow covers contain ice grains in millimeter to submillimeter scales [*Drinkwater*, 1992]. Ice grains are assumed to have a fractional volume of 20%, a correlation function of oblate spheroidal form with correlation lengths $\ell_{1\rho'} = \ell_{1z'}/6 = 1.5 \times 10^{-4}$ m, and random orientations with probability density $p_1(\psi_{1f}, \phi_{1f}) = \sin \psi_{1f}/(4\pi)$. The oblate spheroidal form has been shown to give effective permittivities, calculated from the generalized Polder and van Santen mixing formula in best agreement with measurements [*Sihvola*, 1988].

In the multiyear ice layer the correlation function for ice bubbles is also assumed to be of prolate spheroidal form with correlation lengths $\ell_{2x'} = \ell_{2y'} = \ell_{2z'}/1.5 = 2 \times 10^{-3}$ m and random orientations described by $p_2(\psi_{2f}, \phi_{2f}) = \sin \psi_{2f}/(4\pi)$. The fractional volume of air bubbles is estimated to be 13% from thermodynamic phase equations [*Cox and Weeks*, 1983] based on a density of 800 kg m^{-3}, salinity of 0‰, and temperature of −10°C [*Drinkwater et al.*, 1991b]. Relative permittivity of ice in snow and ice layers at the C band frequency is 3.15 for the real part [*Vant et al.*, 1978] and 1.2×10^{-3} for the imaginary part obtained from an empirical formula [*Tiuri et al.*, 1984]. At L band frequency the real part is 2.95 [*Evans*, 1965] and the imaginary part is 1.3×10^{-3} [*Tiuri et al.*, 1984]. Since multiyear ice is usually very thick, the model for the ice layer is simplified to a half space.

The input parameters for multiyear ice with air inclusions, snow cover, hummocks, and rough interfaces are summarized in Figure 3. From these characterization data, effective

permittivities of the inhomogeneous media are computed, and polarimetric signatures of multiyear ice are calculated with the model and compared with BSFC radar observations.

4.2. Polarimetric Signatures

Conventional backscattering coefficients σ_{hh} and σ_{vv} from multiyear ice in all three sea ice scenes are shown in Figure 4 for C band and Figure 5 for L band. Data for σ_{vv} at 20°–26°

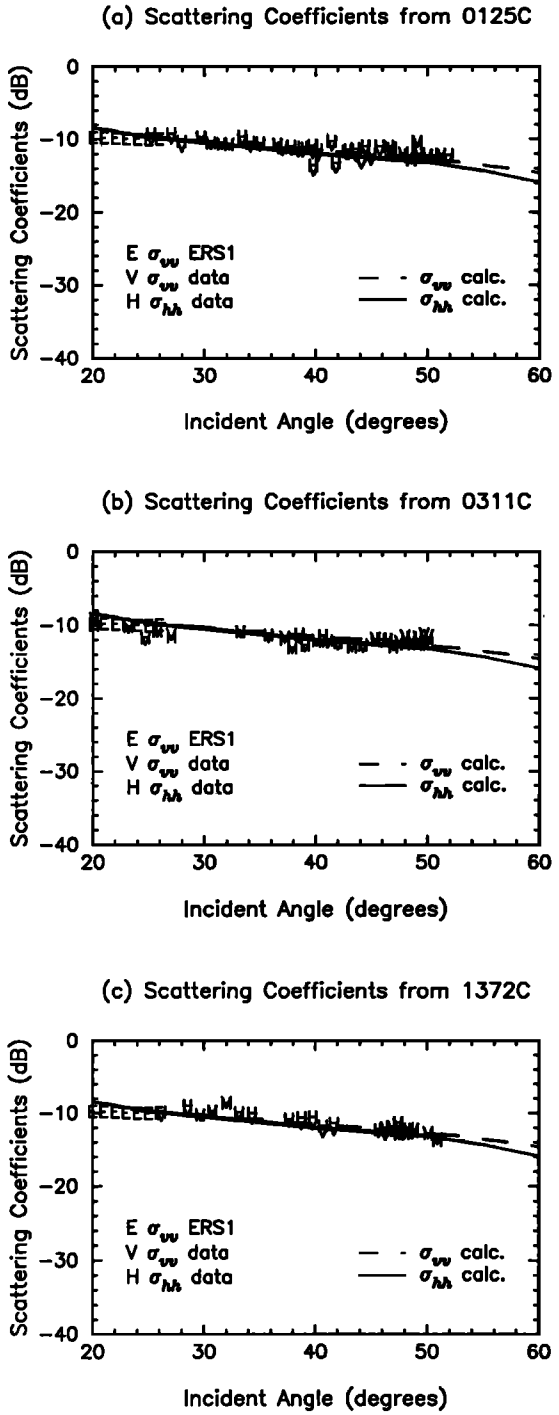

Figure 4. Comparisons of measured and calculated backscattering coefficients at C band for multiyear ice in (a) scene 0125, (b) scene 0311, and (c) scene 1372.

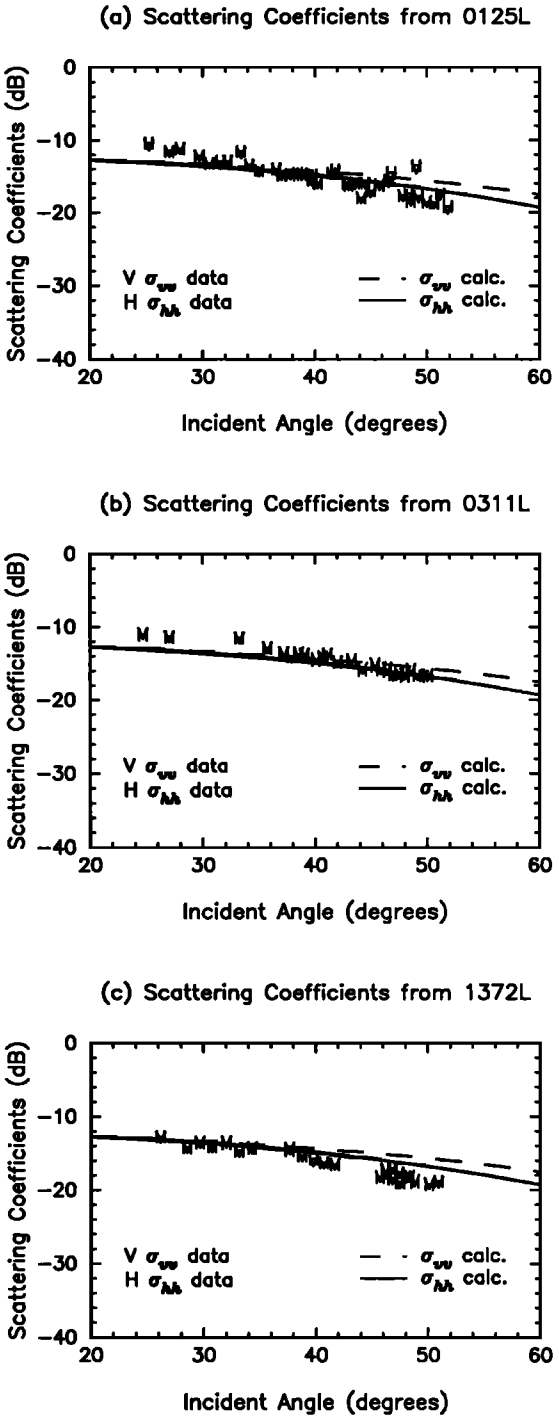

Figure 5. Comparisons of measured and calculated backscattering coefficients at L band for multiyear ice in (a) scene 0125, (b) scene 0311, and (a) scene 1372.

incident angles are from ERS 1 for winter multiyear ice in the Beaufort Sea [*Kwok and Cunningham*, 1994]. Note that backscattering coefficients in this section are plotted on the same scale in all figures for a direct comparison with one another in the discussion of scattering mechanisms. Backscattering coefficients measured by the airborne and spaceborne sensors and theoretical results match well over the range of incident angles under consideration at both frequencies. It is observed that both σ_{hh} and σ_{vv} decrease slowly as

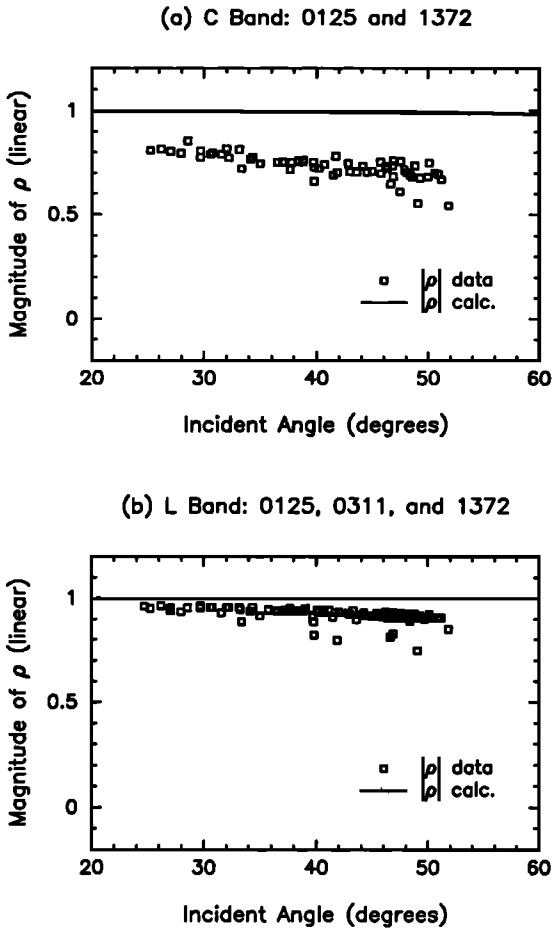

Figure 6. Comparisons of measured and calculated correlation coefficients for multiyear ice at (a) C band and (b) L band.

incident angle increases. Differences between σ_{hh} and σ_{vv} are small, and their ratio γ is therefore close to 1. As discussed in Part 1, these results illustrate isotropic characteristics of multiyear ice due to random orientations of scatterers and weak boundary conditions with small contrasts in effective permittivities of adjacent media. This behavior is rather close to the scattering characteristics from a configuration with centric symmetry [*Nghiem et al.*, 1992].

It is expected from these properties that horizontal and vertical waves are well correlated and correlation coefficient ρ is consequently close to unity with a phase close to zero. Both experimental and theoretical phase angles of ρ are indeed small and thus do not show further informative trends within measurement uncertainty. For magnitude of ρ, the departure from unity in this model is caused mainly by the nonspherical shape of scatterers. Figure 6 compares measured and calculated magnitudes of ρ. At C band, data in Figure 6a are taken only from scenes 0125 and 1372. In scene 0311, processed data contain errors causing discontinuities in phase of ρ, and amplitude of ρ is also affected. It is seen that the measured values of ρ at C band are lower than those calculated.

The difference can be caused by both theory approximations and measurement noises. In the calculation of scattering coefficients, the theoretical model neglects the second and higher orders, which further decorrelate horizontal and vertical waves; this decorrelation effect will lower the magnitude of ρ. At C band, data suffer from a certain level of random noise, which effectively reduces correlation coefficient ρ; the study of noise effects on ρ will be presented below for all of the ice types. Figure 6b compares the magnitude of ρ at L band for multiyear ice. Experimental and theoretical results compare well. Effects of higher order scattering are less at L band than at C band, since the frequency is lower, and noise effects are weaker at L band; therefore horizontal and vertical waves are well correlated, as explained by the model.

Contributions to total scattering signatures of multiyear ice are studied by considering components due to different scattering mechanisms. Figure 7 presents results at vertical polarization. Results at horizontal polarization are similar and are not shown here. As seen in Figure 7a for C band, scattering at incident angles larger than 30° is from volume inhomogeneities. Surface scattering is important at smaller incident angles. Effects of hummocks also start to appear at incident angles higher than 60°, where the total scattering is larger than the volume scattering without hummocks (dotted curve in Figure 7a). L band results in Figure 7b reveal similar trends with the volume-surface scattering transition at 20° incident angle instead of 30° at C band.

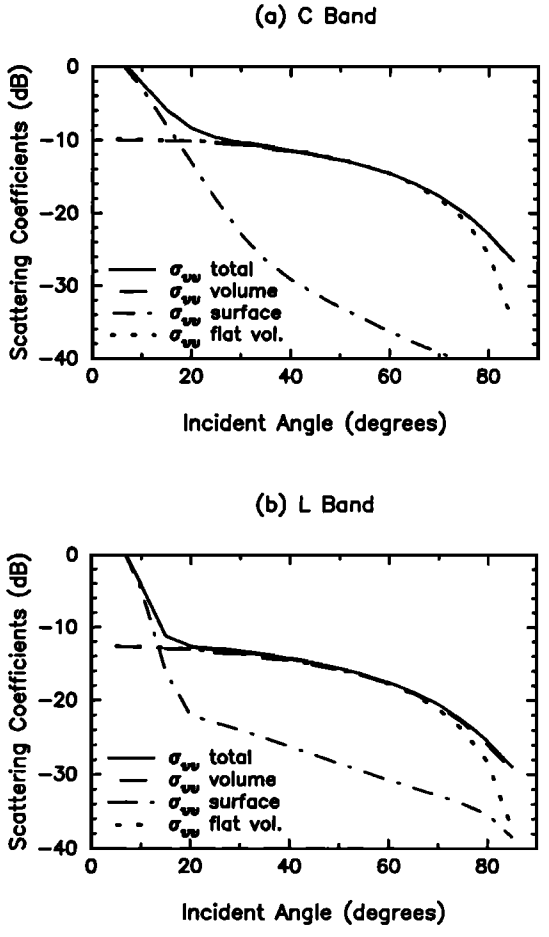

Figure 7. Composition of scattering from sea ice for (a) C band and (b) L band. Solid curves are total, dashed curves are volume scattering with effects of hummocks, dash-dotted curves are surface scattering with both small-scale roughness and large-scale hummocks, and dotted curves are volume scattering with flat interfaces.

In Figure 8, various components contributing to surface scattering are investigated at small incident angles where surface mechanisms are dominant. For scattering from the snow-ice interface, the small-scale component is calculated by removing the hummock roughness from the model, and the hummock backscattering component is obtained by subtracting the small-scale contribution from the total surface scattering. In Figure 8a for C band, the snow-ice interface dominates surface scattering for incident angles up to 28°, where air-snow surface scattering becomes significant. At this angle, however, volume scattering starts to take over the total scattering, as shown in Figure 7a.

At incident angles smaller than 20° in Figure 8a, the contribution of the small-scale component to snow-ice surface scattering is larger; however, both hummocks and small-scale roughness contribute almost equally to the total surface scattering from snow-ice interface at incident angles larger than 20°. Overall, these two components show the same trend along the range of incident angles under consideration. Behavior of surface scattering at L band is different, as seen in Figure 8b; the snow-ice component dominates the air-snow component, which decreases quickly with incident

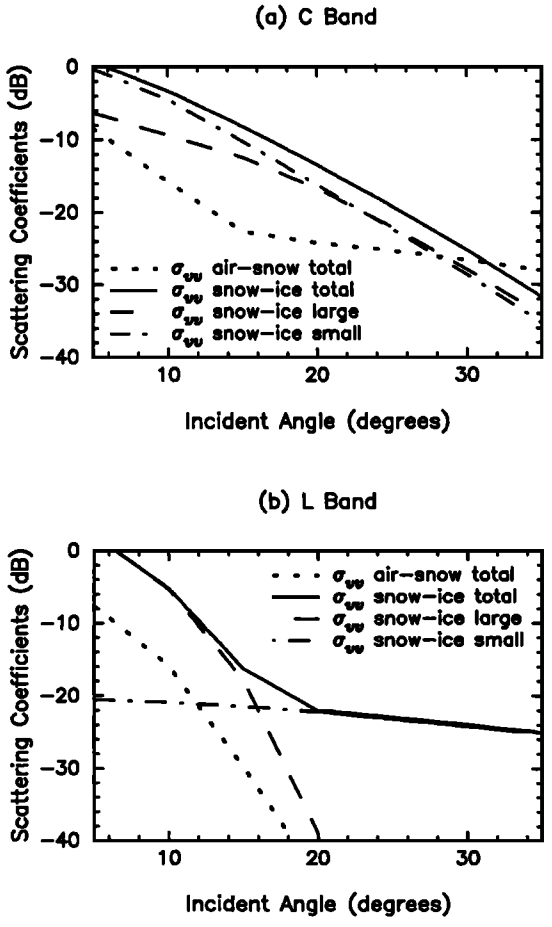

Figure 8. Composition of surface scattering at small incident angles for (a) C band and (b) L band. Dotted curves are total surface scattering from air-snow interface. For snow-ice interface, solid curves are for total surface scattering, dashed curves are scattering from large-scale roughness due to hummocks, and dash-dotted curves are scattering from small-scale roughness.

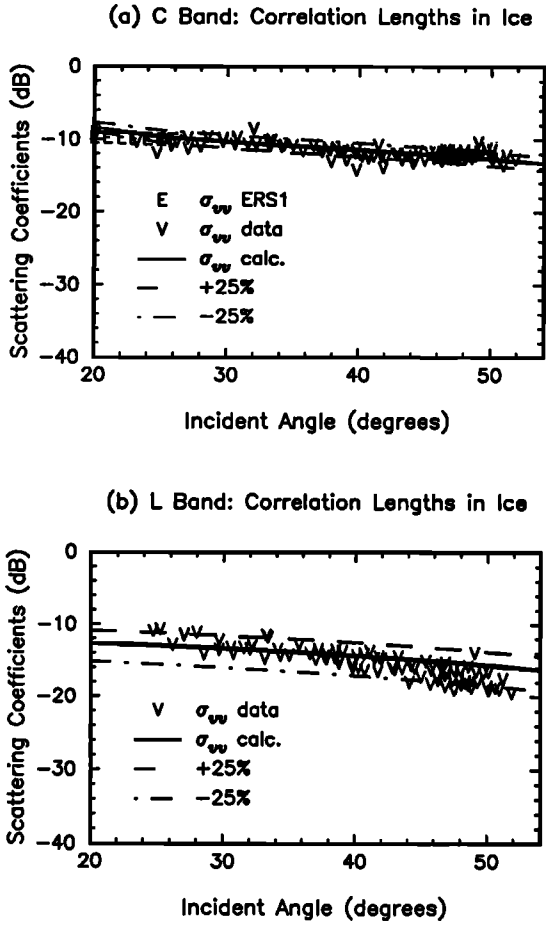

Figure 9. Variations in calculated backscattering coefficients due to ±25% change in correlation lengths of air inclusions for (a) C band and (b) L band.

angle. For snow-ice total surface scattering, the large-scale hummock component quickly decreases with increasing incident angle and becomes dominated at incident angles larger than 20° by the slower decreasing small-scale component. The roughness of the composite surface, which contains different scales, is perceived differently at L band, whose wavelength is more than 4 times longer than that at C band. Therefore, in general, the surface appears smoother at L band and the backscattering coefficients decrease faster at small incident angles compared with those at C band. This is not surprising because the backscattering pattern as a function of incident angle should spread to larger incident angles for rougher surface with more diffuse scattering, while the pattern for a smoother surface should be more limited to smaller incident angles.

4.3. Sensitivity Analysis

There are always uncertainties due to inaccuracies in measurements or lack of in situ information. Thus signature sensitivity needs to be analyzed to study variations caused by different input parameters. To calculate polarimetric backscattering coefficients for comparison with measurements, correlation lengths for air inclusions in the multiyear ice layer are estimated. Variations in scattering coefficients due to the uncertainty in these correlation lengths are shown in Figure 9, where continuous curves are for the original

correlation lengths, dashed curves for correlation lengths increased by 25%, and dash-dotted curves for a reduction in correlation lengths also by 25%; both JPL SAR and ERS 1 data are plotted for comparison. Results suggest that the variance due to correlation lengths is larger at L band when compared with C band; Figure 9 reveals a larger spread at L band compared with C band.

The volume scattering contribution from the snow layer is small when compared with other terms in the total scattering, indicating that correlation lengths of ice grains in snow have little influence upon the total backscattering in this case. The sensitivity to surface parameters is also investigated at both C band and L band. For C band a variation of 25% in small-scale and hummock surface correlation lengths at the snow-ice interface can give a change of 2 dB at 20° incident angle. For L band a variation of 25% in hummock correlation length can result in a change of 3 dB at 15°, where scattering from the hummock surface is important.

5. First-Year Sea Ice

5.1. Characterization Parameters

In contrast to multiyear ice, first-year ice does not have melt hummocks. During Arctic winter, both first-year and multiyear ice were covered by a snow layer, and snow characterization parameters are therefore kept the same as in the last section. The snow-ice interface has a small-scale roughness of $\sigma_{12r} = 2.8 \times 10^{-3}$ m and $\ell_{12r} = 8.0 \times 10^{-2}$ m obtained from surface profiles measured during the BSI1 campaign by *Carlström* [1992] and M. R. Drinkwater (unpublished data, 1990). Detailed roughness characterization of the underside of thick first-year ice, which will be modeled as a planar interface, is not available. However, incident field strength is weak at the ice-water interface due to the attenuation in thick first-year saline ice.

Thickness of the first-year ice layer is between 1.5 and 2.4 m as measured at the APLIS ice station [*Wen et al.*, 1989]; thus an average of 2.0 m is used in the model for thick first-year sea ice. Near the APLIS station, first-year ice was in a frozen lead, as seen in Figure 2b. From many field measurements, *Cox and Weeks* [1974] deduce an empirical linear relation between salinity and ice thickness. The relationship is given by $S = 7.88 - 1.59h$ for cold sea ice, where S is salinity in parts per thousand and h is ice layer thickness in meters. This relationship is consistent with a bulk salinity of 7.3‰ for 0.43-m-thick first-year ice in a frozen lead measured by *Gow et al.* [1990]. At $h = 2.0$ m the corresponding salinity is 4.7‰ from Cox and Weeks' salinity relation. For an average temperature of −10°C and bulk ice density of 920 kg m^{-3} reported by *Drinkwater et al.* [1991b] for the Beaufort first-year sea ice, *Cox and Weeks*'s [1983] phase equations yield a brine fractional volume of 2.6% and a negligible air fractional volume of 0.4%.

The fractional volume of brine inclusions in the upper meter of the first-year ice layer is reported between 1.9% and 3.2%, according to APLIS data obtained by *Wen et al.* [1989]. Thus the brine volume $f_{2s} = 2.6\%$ is about the average of the APLIS brine range above and will be used in theoretical calculations. Note that another salinity relation, $S = 1.57 + 0.18h$ [*Meese*, 1989], gives a different constituent phase distribution in sea ice for the same thickness and thus results in different signatures. This relation, however, is

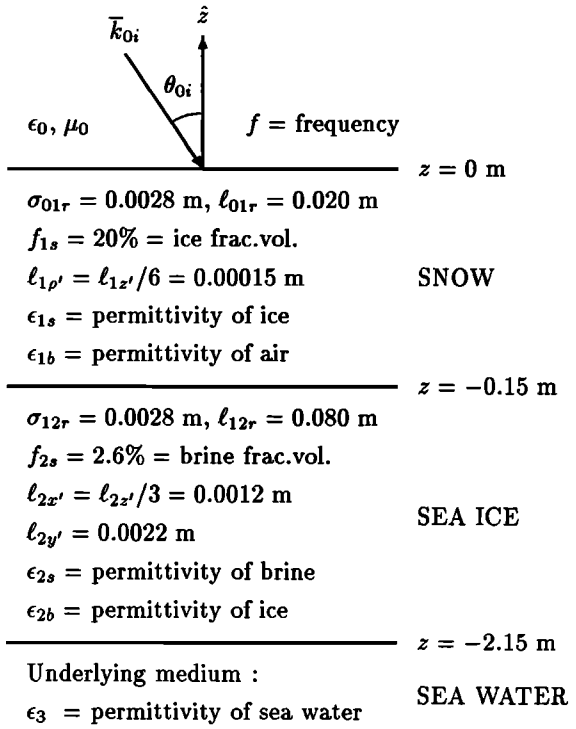

Figure 10. Physical parameters for first-year sea ice.

for warm sea ice, which is inappropriate for winter ice conditions described in this paper.

Brine inclusions of millimeter size have a substantially ellipsoidal form, as seen from horizontal thin sections of sea ice [*Weeks and Ackley*, 1982; *Arcone et al.*, 1986; *Gow et al.*, 1987]. Correlation lengths for brine inclusions in first-year ice are taken to be $\ell_{2x'} = \ell_{2z'}/3 = 1.2 \times 10^{-3}$ m and $\ell_{2y'} = 2.2 \times 10^{-3}$ m to describe the ellipsoidal shape. As indicated in Part 1, crystallographic structure in columnar ice renders a preferential alignment of brine inclusions in the vertical direction with random azimuthal orientations. This orientation distribution is depicted with a probability density function of the form $p_2(\psi_{2f}, \phi_{2f}) = \delta(\psi_{2f})/(2\pi)$.

Permittivities of brine [*Stogryn and Desargant*, 1985] at −10°C are $\varepsilon_{2b} = (42.0 + i44.5)\varepsilon_0$ at the C band frequency of 5.3 GHz and $\varepsilon_{2b} = (53.6 + i107.4)\varepsilon_0$ at the L band frequency of 1.25 GHz. Permittivities of the ice background are $\varepsilon_{2b} = (3.15 + i0.0012)\varepsilon_0$ [*Vant et al.*, 1978; *Tiuri et al.*, 1984] at C band and $\varepsilon_{2b} = (2.95 + i0.0013)\varepsilon_0$ [*Evans*, 1965; *Tiuri et al.*, 1984] at L band. For seawater the temperature was about −2°C, and the salinity ranged between 31‰ and 35‰ [*Wen et al.*, 1989]. From a formula based on the Debye equation [*Klein and Swift*, 1977], permittivities of the seawater are estimated as $\varepsilon_3 = (60 + i40)\varepsilon_0$ at C band and $\varepsilon_3 = (76 + i50)\varepsilon_0$ at L band.

The above characterization parameters for first-year sea ice are summarized in Figure 10 and used to obtain polarimetric signatures from the model.

5.2. Polarimetric Signatures

Results for conventional backscattering coefficients σ_{hh}, σ_{vv}, and σ_{hv} are presented in Figures 11 and 12 at C and L bands, respectively. In addition to JPL SAR signatures, ERS 1 data for σ_{vv} of typical undeformed first-year ice are included at C band. Measured and calculated values are in good

agreement for all three scattering coefficients at both frequencies over the range of incident angles under consideration. The general trends are a slow decrease in backscattering coefficients with increasing incident angle, a small difference between σ_{hh} and σ_{vv}, and σ_{hv} about 16 dB below copolarized returns.

Cross-polarized backscattering coefficient σ_{hv} is obtained under the first-order distorted Born approximation in this model due to the ellipsoidal shape of brine inclusions.

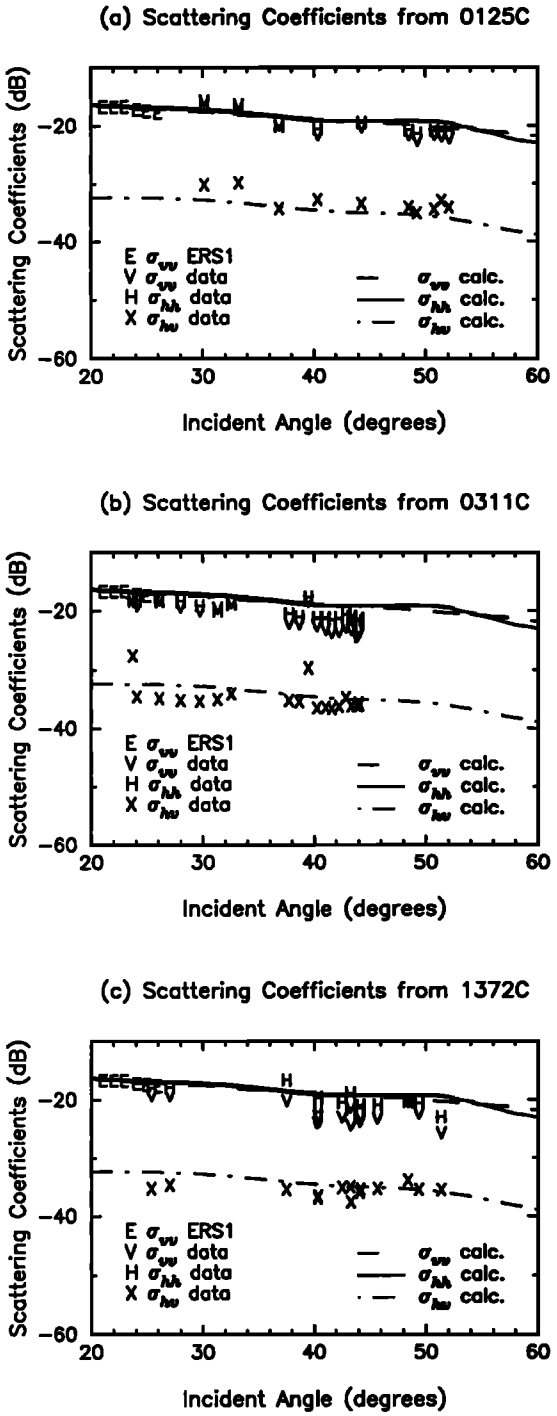

Figure 11. Comparisons of measured and calculated backscattering coefficients at C band for first-year ice in (a) scene 0125, (b) scene 0311, and (a) scene 1372.

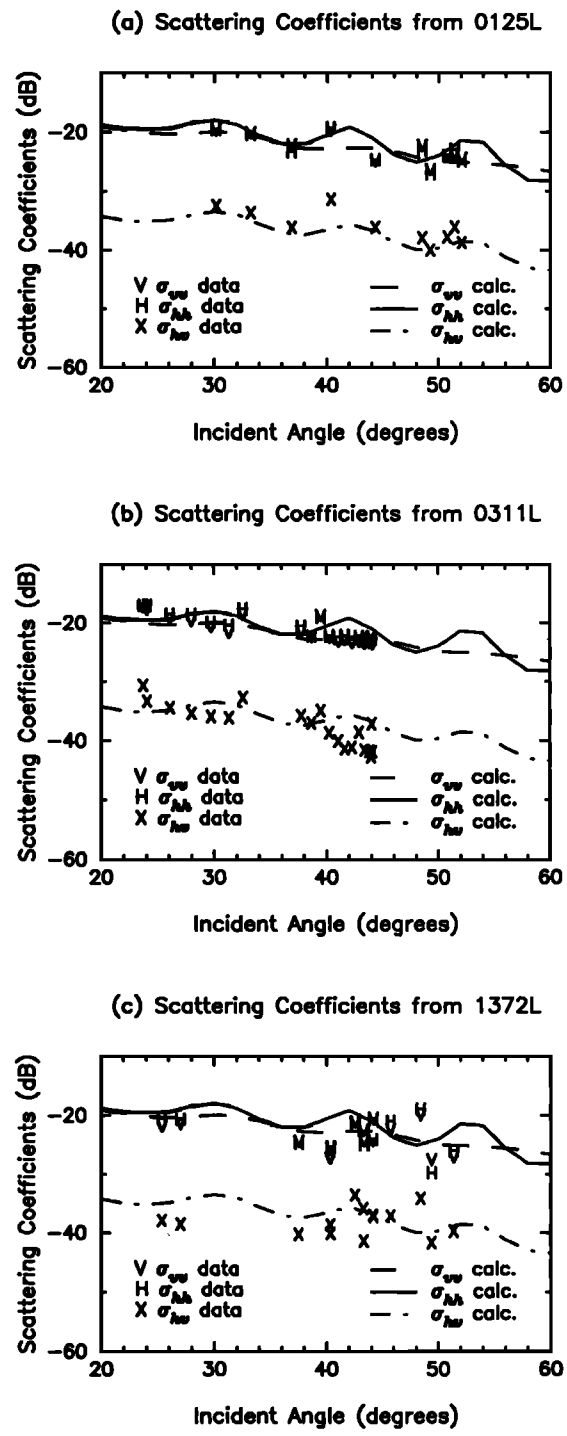

Figure 12. Comparisons of measured and calculated backscattering coefficients at L band for first-year ice in (a) scene 0125, (b) scene 0311, and (a) scene 1372.

Oscillations observed in theoretical curves are due to boundary effects, which diminish if an averaging process is taken over variations in layer thicknesses. Total surface scattering is lower than that from ice grains and brine inclusions, especially at larger incident angles. The contribution from surface scattering is calculated from the Kirchhoff approximation with the measured roughness parameters for first-year ice in the Beaufort Sea.

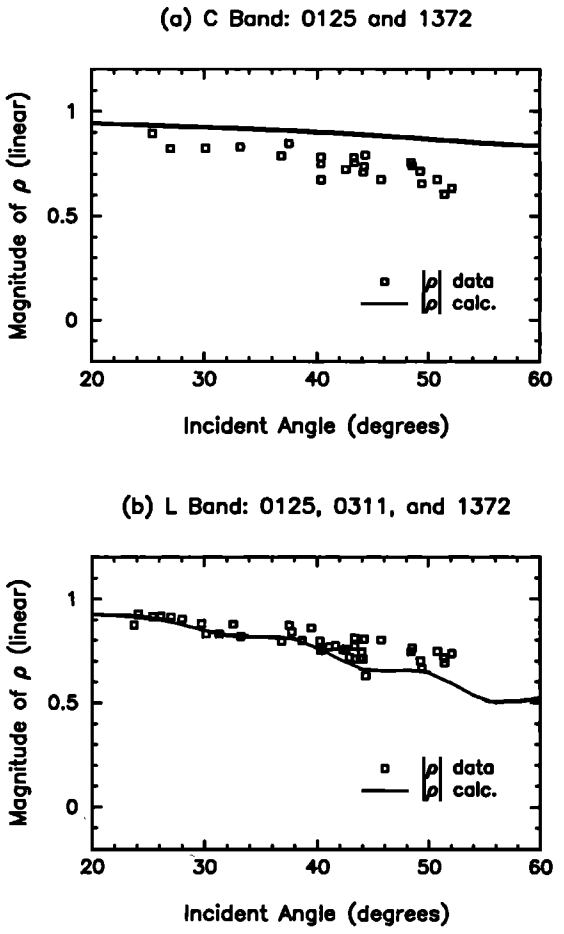

Figure 13. Comparisons of measured and calculated correlation coefficients for first-year ice at (a) *C* band and (b) *L* band.

Magnitudes of correlation coefficient ρ are shown in Figure 13. Decorrelation between horizontal and vertical waves is illustrated by ρ whose magnitude is lower than unity. In the present model this is explained by two effects: (1) ellipsoidal shape of brine inclusions and (2) anisotropy due to the preferential vertical orientation of brine pockets. The anisotropy is manifested in both real and imaginary parts of permittivities for horizontal (ordinary) and vertical (extraordinary) waves. The difference in the real parts is responsible for the difference in wave speeds, and the imaginary parts for the wave attenuations. These differences affect amplitudes of the horizontal and vertical waves, separate scattering centers of the two characteristic waves, and together with the ellipsoidal shape, contribute to the overall decorrelation effect.

Figure 13a presents ρ results at *C* band. Measured values are lower than theoretical calculations. This can be caused by noise effects as discussed in the case of multiyear ice. High order scattering can also reduce magnitude of ρ; however, the high order contribution in first-year ice is less important than that in multiyear ice because first-year ice has sparser scatterers and more absorption loss. Measured and calculated magnitudes of ρ at *L* band are close, as seen in Figure 13b. Compared with multiyear ice at *L* band, magnitude of ρ for first-year ice is lower and well separated, especially at larger incident angles.

5.3. Sensitivity Analysis

To assess effects of various sea ice characterization parameters on first-year ice signatures, a sensitivity study is carried out by varying these parameters and observing corresponding changes in the predicted signatures. The size of brine inclusions, modeled by correlation lengths, in sea ice can be changed due to the sea ice growth process (section 2.4, Part 1) and thermal modification [*Gow et al.*, 1987]. The scatterer size can also vary at different locations in a sea ice area. The correlation lengths used in the data comparison are varied by ±25% in this investigation.

Results in Figure 14a for *C* band reveal a variation of 1 dB in σ_{vv}, where JPL SAR and ERS 1 data are also shown, in inverse relation to the change in scatterer correlation lengths. When scatterer size increases, scattering effect becomes stronger and scattering loss becomes more severe. These effects are inherently related (section 2.1, Part 1). Thus backscattering coefficients are increased by larger scatterers on the one hand; however, scattering effects are decreased by stronger attenuation on the other hand. These competing effects can cause the inverse relation between the backscatter and the scatterer size at *C* band, where scattering loss is important. For *L* band, Figure 14b indicates a direct relation in the variations between scatterer size and

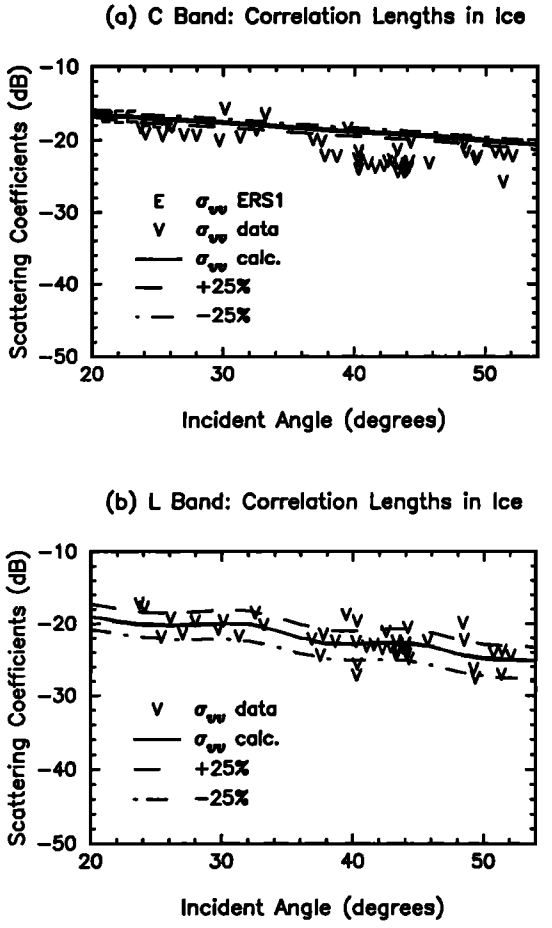

Figure 14. Variations in calculated backscattering coefficients due to ±25% change in correlation lengths of brine inclusions for (a) *C* band and (b) *L* band.

backscattering coefficient σ_{vv}, which can be changed as much as 3 dB for a 25% change in correlation lengths.

Coefficients σ_{hv} and ρ are related to the shape of brine inclusions. Scatterer shape is represented by correlation length ratios $\ell_{2y'}/\ell_{2x'}$ and $\ell_{2z'}/\ell_{2x'}$ in the model. As seen in Figure 15, σ_{hv} is sensitive to changes in correlation length ratios or scatterer shape at both C band and L band frequencies. For magnitude of ρ, the variations are larger at L band than at C band, as seen in Figure 16 when correlation length ratios are varied.

6. Thin Lead Ice

6.1. Characterization Parameters

Divergent ice motion creates leads as discussed in section 3.1. From APLIS records [*Wen et al.*, 1989], ice drift at high velocity started late on March 10, reached the maximum above 32 cm s^{-1} early on March 11, remained close to 20 cm s^{-1} until about 10 geomagnetic time (GMT), then subsided to below 5 cm s^{-1}. Leads observed in scene 1372 (Figure 2c) were acquired at 17.3 GMT on March 11, 1988. For Arctic sea ice, the growth rate on March 11 [*Thorndike et al.*, 1975] is shown in Figure 4 of Part 1. Integrated over this growth, a thickness of less than 4 cm is obtained for a 7-hour period (see middle curve for sea ice in Figure 4b, Part 1). Thus an estimated average thickness of 3.5 cm for the thin ice layer is

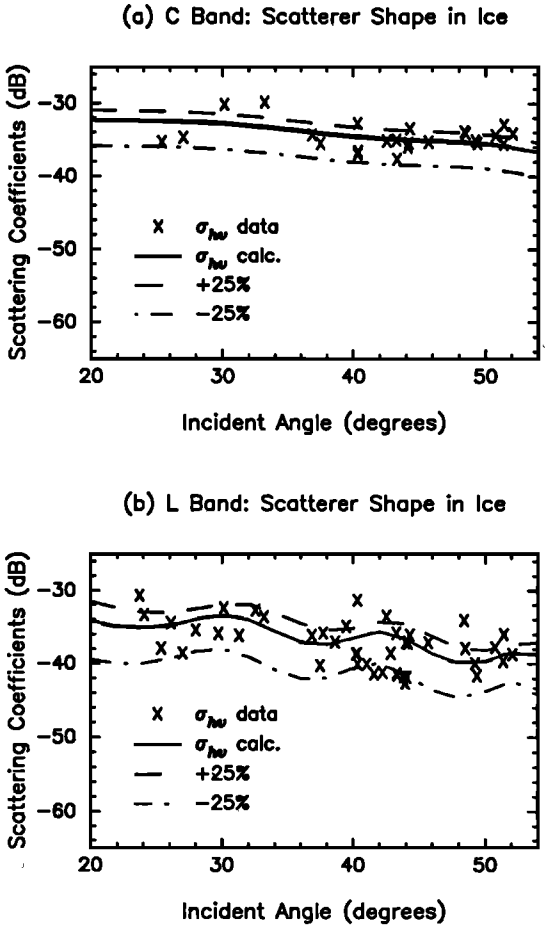

Figure 15. Variations in calculated backscattering coefficients due to ±25% change in ratios of brine correlation lengths for (a) C band and (b) L band.

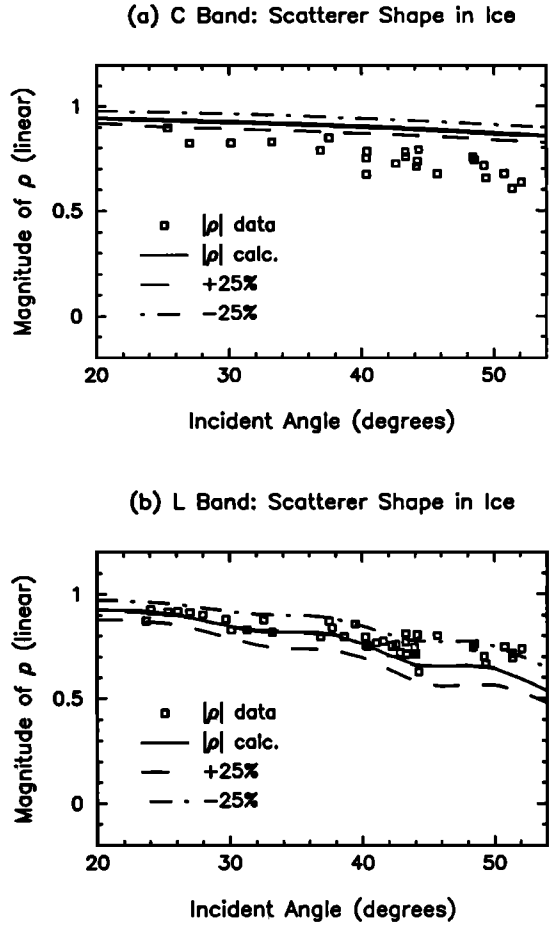

Figure 16. Variations in calculated correlation coefficients due to ±25% change in ratios of brine correlation lengths for (a) C band and (b) L band.

used in the model. Furthermore, a gamma distribution of the form $q_2(h) = (d_2/\mu_h)\exp(-d_2/\mu_h)$ is assumed for variations in thickness h with a mean of $2\mu_h$. Thickness distribution is determined by variations in growth rate, sea ice dynamics, and other environmental effects (section 3.2, Part 1).

Field measurements in the Beaufort Sea indicate that thin ice at a thickness of a few centimeters can have a bulk salinity as high as 16‰ [*Cox and Weeks*, 1974]. For thin ice less than 0.4 m in thickness, *Cox and Weeks* [1974] found an empirical linear relation between salinity S and thickness h given by $S = 14.24 - 19.39h$, which suggests $S = 13.6$‰ at a thickness of 3.5 cm. Saline ice grown in a cold room during CRRELEX (September 1993) from 30‰ saline water at an air temperature of −22°C has a salinity of 14‰ for 3.5-cm-thick ice. Based on these estimations, a salinity of 15‰ is selected for theoretical calculations. At an average temperature of −8°C [*Drinkwater et al.*, 1991b] the volume fraction of brine inclusions is 10% as obtained from *Cox and Weeks*'s [1983] phase equations without gaseous constituent.

In the sea ice layer, relative permittivities are $\varepsilon_{2s} = 45.3 + i44.8$ [*Stogryn and Desargant*, 1985] for brine inclusions and $\varepsilon_{2b} = 3.15 + i0.0013$ [*Vant et al.*, 1978; *Tiuri et al.*, 1984] for ice background at C band. Those at L band are $\varepsilon_{2s} = 57.3 + i103.0$ [*Stogryn and Desargant*, 1985] and $\varepsilon_{2b} = 2.95 + i0.0014$ [*Evans*, 1965; *Tiuri et al.*, 1984] for brine and ice, respectively. Brine inclusions in thin ice are

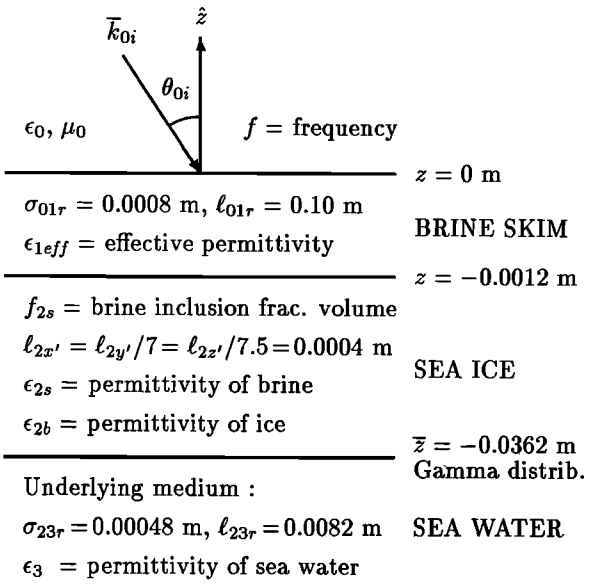

Figure 17. Physical parameters for thin lead ice.

described with correlation lengths $\ell_{2x'} = \ell_{2y'}/7 = \ell_{2z'}/7.5 = 4.0 \times 10^{-4}$ m for the ellipsoidal form with orientation probability density $p_2(\psi_{2f}, \phi_{2f}) = \delta(\psi_{2f})/(2\pi)$.

It has been observed during LeadEx and in other locations that there exists a thin and highly saline skim on new ice surface [*Perovich and Richter-Menge*, 1994; *Drinkwater and Crocker*, 1988]. This is a slushy layer of the order of millimeter thick and composed of ice and brine with salinity as high as 100‰. Due to the high salinity, the surface brine layer has a high permittivity and significantly affects polarimetric signatures of the thin ice (section 3.2, Part 1). The surface brine skim is assumed to be a mixture of ice and brine with a thickness of 1.2×10^{-3} m and effective permittivities of $\varepsilon_{1eff} = (12.9 + i9.2)\varepsilon_0$ at C band and $\varepsilon_{1eff} = (15.9 + i21.1)\varepsilon_0$ at L band. These are estimated by Polder and van Santen's mixing formula, which can be reduced from strong fluctuation results in the low-frequency limit [*Tsang et al.*, 1985], for spherical scatterers with constituent fractional volumes calculated from salinity and temperature in the brine layer. Volume scattering in this thin and high loss layer is ignored in this model.

At the interface between air and the brine layer, the surface is imposed by a roughness with $\sigma_{01r} = 8.0 \times 10^{-4}$ m and $\ell_{01r} = 0.1$ m, while the interface between brine and ice layers is smooth. The underside of the ice layer naturally has some small-scale roughness which has not been well characterized for Arctic thin lead ice. Roughness measurements of an ice underside were obtained from CRRELEX, and the results reported a height standard deviation of $\sigma_{23r} = 4.8 \times 10^{-4}$ m and a correlation length of $\ell_{23r} = 8.2 \times 10^{-3}$ m [*Onstott*, 1990]. Below this interface is seawater with high relative permittivities (obtained previously in the case for first-year ice in section 5.1).

Figure 17 lists physical parameters of thin ice used in the model. The composite model with both volume and surface scattering mechanisms under effects of the slushy brine layer is used to simultaneously explain all the trends observed in complete sets of polarimetric scattering coefficients at both C band and L band frequencies.

6.2. Polarimetric Signatures

Results for polarimetric backscattering coefficients and complex correlation coefficients are shown in Figures 18 and 19, where theoretical calculations and experimental data are compared. For C band results in Figure 18, it is observed that σ_{vv} decreases by approximately 5 dB over the range of incident angles, while the decreasing slope in σ_{hh} is even

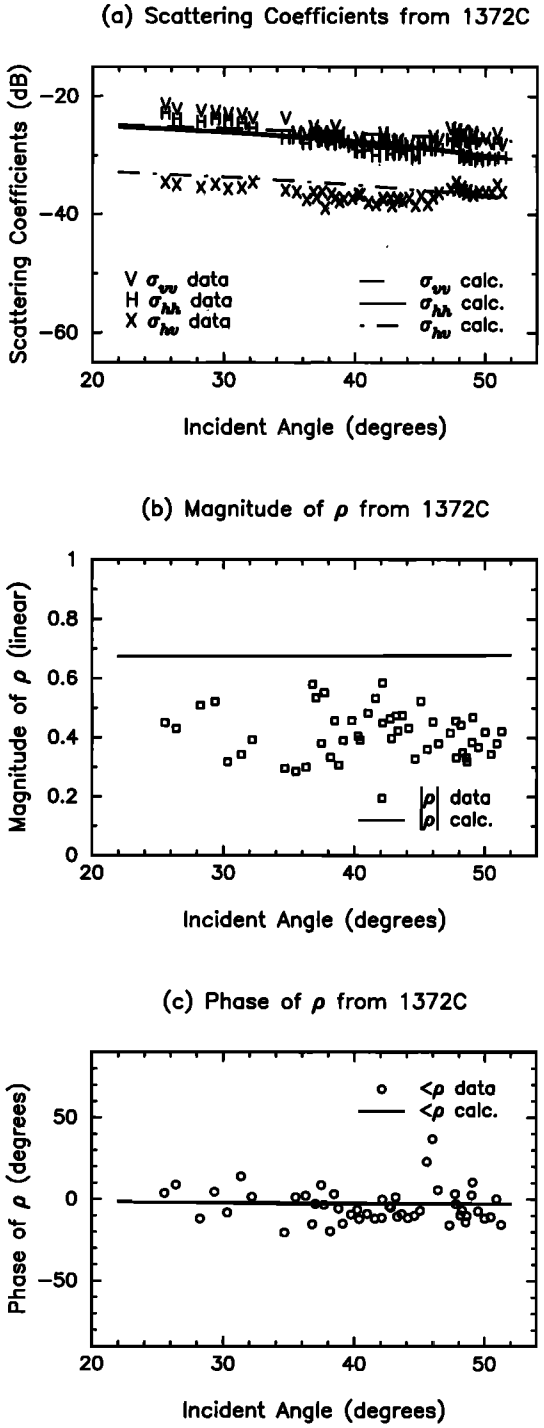

Figure 18. Comparisons of measured and calculated backscattering and correlation coefficients for thin lead ice at C band for (a) conventional backscattering coefficients, (b) magnitude of correlation coefficient, and (c) phase of correlation coefficient.

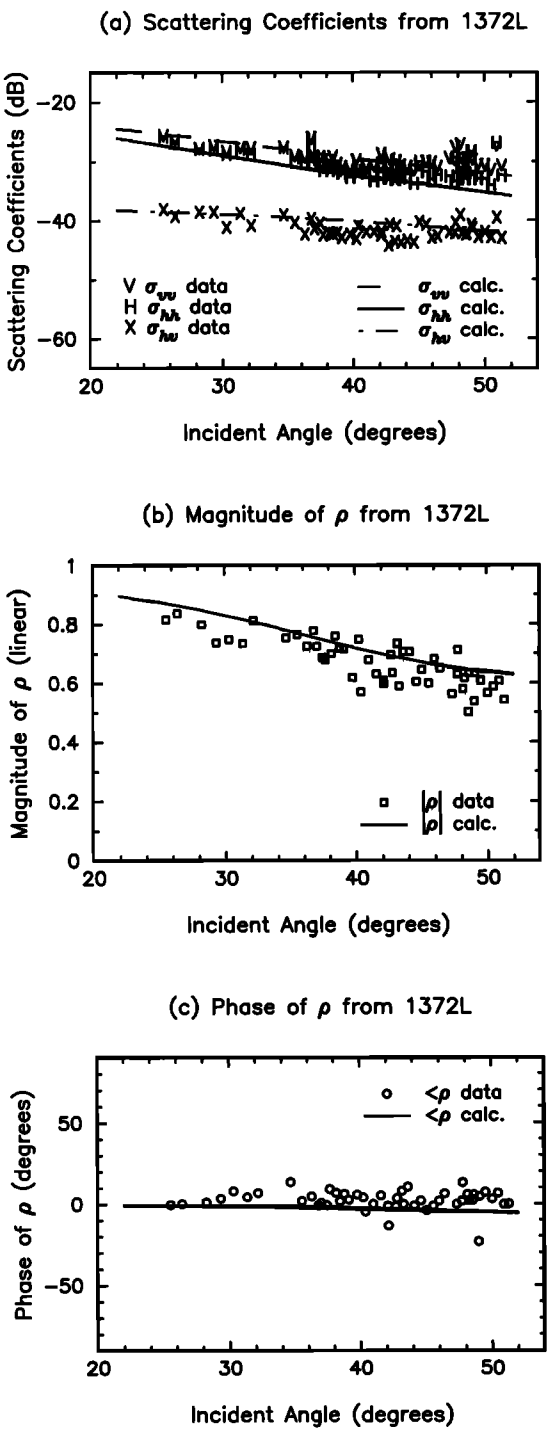

Figure 19. Comparisons of measured and calculated backscattering and correlation coefficients for thin lead ice at L band for (a) conventional backscattering coefficients, (b) magnitude of correlation coefficient, and (c) phase of correlation coefficient.

steeper. Scattering coefficient σ_{vv} is higher than σ_{hh}, and copolarization ratio $\gamma = \sigma_{vv}/\sigma_{hh}$ is small at small incident angles and increases to more than 3 dB at large incident angles. These copolarized data match the calculations except that theoretical values are lower at small incident angles. Cross-polarized returns are compared with the calculations, which are a little higher than experimental data (Figure 18a).

The magnitude of ρ of the lead ice at C band is low when compared to first-year and multi-year ice, and is insensitive to incident angles as seen in Figure 18b. The measured values spread between 0.3 and 0.6 and are lower than the calculated values of about 0.65. This is because returns from thin ice are low at C band and thus the decorrelation effects of noise are more severe. In Figure 18c, measured and theoretical phases of ρ are small and show a slightly decreasing trend.

Figure 19a for L band shows that copolarized returns σ_{vv} and σ_{hh} decrease quickly as functions of incident angles, and copolarized ratio γ is large at large incident angles. Cross-polarized returns in Figure 19a reveal a slightly decreasing trend as incident angles increase. Except for some high data points, which can be caused by localized differences in sea ice thickness and characteristics or by some data pixels of older ice near the lead edges, the comparison of the overall levels and trends between measured and theoretical results is good for these conventional backscattering coefficients.

In contrast to the behavior of the magnitude of ρ measured at C band, ρ at L band clearly shows a decrease in magnitude with increasing incident angles as seen in Figure 19b. Phases of ρ at L band are small and insensitive to incident angles. Both magnitudes in Figure 19b and phases in Figure 19c of complex coefficient ρ are well compared with model results. In general, the composite model with the brine layer, volume, and surface scattering mechanisms simultaneously matches the trends observed in measured polarimetric signatures at both C band and L band frequencies.

To provide physical insights into the behavior of polarimetric backscattering signatures of thin ice, scattering mechanisms in the layered configuration are investigated. If the total scattering is completely due to volume scattering without surface contribution, backscattering coefficients σ_{vv} and σ_{hh} at L band are too low, especially at small incident angles and decrease slowly as functions of incident angle in theoretical calculations, in contrast to experimental observations as seen in Figure 20a. Furthermore, the theoretical magnitude of ρ (Figure 20b) does not have the strong decreasing trend observed in the data as presented in Figure 19b. In this case, surface scattering is dominant at small incident angles, is comparable to volume scattering at about 30° incident angle, and still has some contribution at larger incident angles. Surface scattering also contributes to the total scattering at C band, but the relative contribution is smaller.

On the other hand, surface scattering alone without volume scattering cannot explain low values of the magnitude of ρ in measurements at both frequencies, as shown in Figure 21. The low magnitudes of ρ are caused by a decorrelation effect of ellipsoidal scatterers in the anisotropic layered configuration. It has been indicated that noise can contribute to this decorrelation; however, an unduly large amount of noise in copolarized signals is necessary to take the magnitude of ρ calculated from surface scattering alone down to the level of measured data. Thus the decrease in magnitude of ρ at L band is caused by a combination of both rough surfaces and ellipsoidal scatterers. If the scatterers become spherical, vertical and horizontal returns are more correlated, as suggested by the larger magnitude of ρ in Figure 22.

For the brine layer, the effect is that the high permittivity preferentially enhances the reflection of energy in horizontal

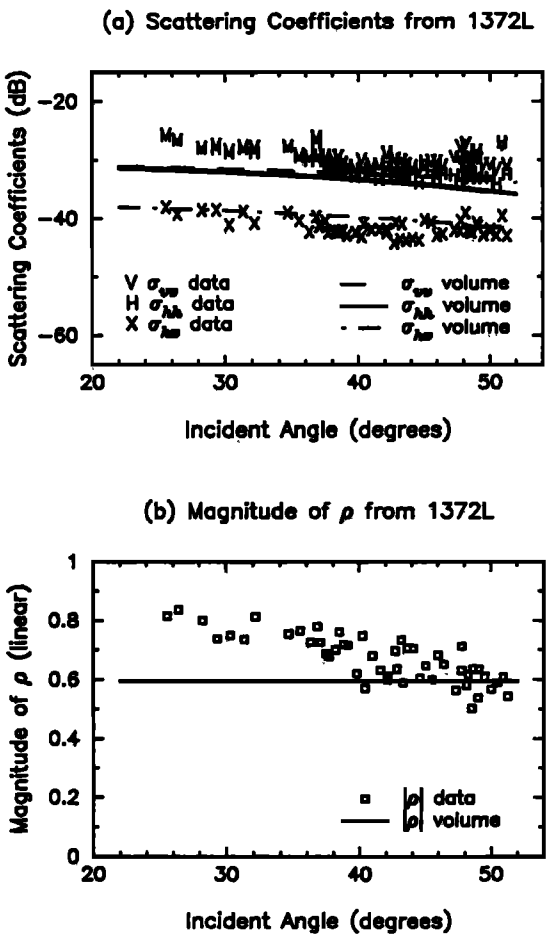

Figure 20. Comparisons of measured and calculated backscattering and correlation coefficients for thin lead ice at C band for (a) conventional backscattering coefficients, (b) magnitude of correlation coefficient. The calculations are for volume scattering without surface scattering.

polarization. Consequently, transmission in horizontal polarization is less compared with the vertical, reducing backscattering coefficient σ_{hh} relative to σ_{vv}, and thus copolarized ratio γ becomes larger, especially at larger incident angles. Without the brine layer, the calculated values of γ at C band are less than 1 dB at about 50° incident angle, while the measurement is larger than 3 dB. At L band without the brine layer, the trend in γ is reversed: calculated γ is negative in dB ($\gamma < 1$ in linear scale), while measured data are about 3 dB at 50° incident angle. This indicates that the brine layer is necessary to explain observed values of copolarized ratio γ.

6.3. Sensitivity Analysis

To study the uncertainty due to correlation lengths of brine inclusions, a simulation is carried out by varying the lengths by factors of 0.75 and 1.25 (or ±25%). Results are presented in Figure 23a for C band and Figure 23b for L band. There are three curves for each backscattering coefficient σ_{vv}, σ_{hh}, or σ_{hv}. The middle curve is calculated from the correlation lengths used in the data comparison, the upper is for the 25% increase, and the lower for the 25% decrease.

The plots show that backscattering coefficients at L band, when compared with C band, are more sensitive to these correlation lengths. Moreover, copolarized returns σ_{vv} and σ_{hh} at L band have smaller variations at smaller incident angles as compared with the change in cross-polarized return σ_{hv}, as seen in Figure 23b. The reason is that all cross-polarized backscattering coefficients are calculated from ellipsoidal scatterers, while copolarized returns contain contributions from both volume and surface scattering mechanisms. L band returns at smaller incident angles are also sensitive to rough surface parameters such as height standard deviation and surface correlation length.

7. Effects of Noise

Noise effects on correlation coefficient ρ are studied in this section for the different ice types. The correlation between horizontal and vertical returns can be reduced by system noise, which is assumed to be independent of the scattering signal from sea ice. Also, the noise is not correlated between horizontal and vertical channels, which are balanced in noise amplitude. In this case, noisy correlation coefficient ρ_n is related to the true correlation coefficient ρ of sea ice by

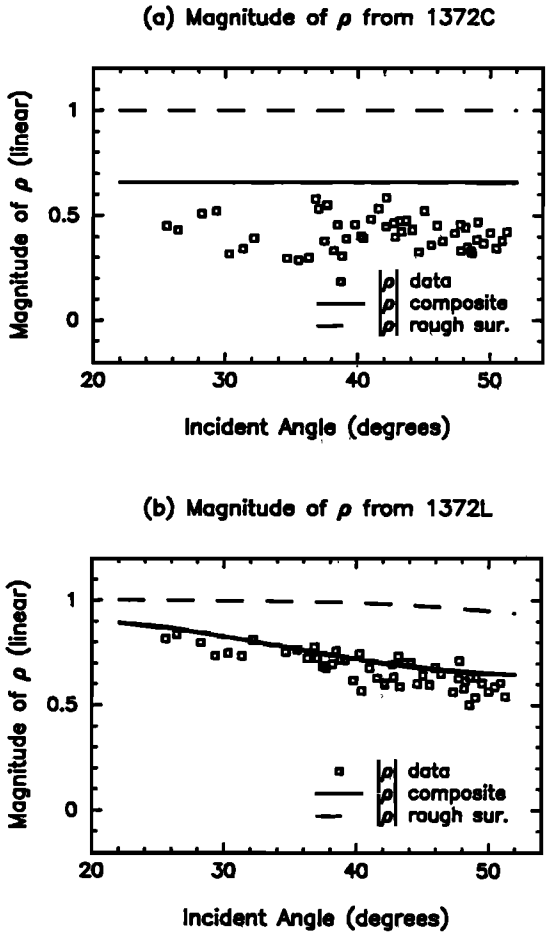

Figure 21. Comparisons of measured and calculated correlation coefficients for thin lead ice at (a) C band and (b) L band. Solid curves are calculated from the complete composite model. Dashed curves are for surface scattering without volume scattering.

$$\rho_n = \rho\left[\left(1+\frac{1}{\mathrm{SNR}_0}\right)\left(1+\frac{1}{\gamma\mathrm{SNR}_0}\right)\right]^{-1/2}$$

where SNR_0 is the signal-to-noise ratio defined with a reference (ref) in σ_{hh} and the noise σ_n as $\mathrm{SNR}_0 = \mathrm{ref}(\sigma_{hh})/\sigma_n$.

Correlation coefficient ρ influenced by noise effects is shown in Figure 24 for multiyear ice where $\mathrm{ref}(\sigma_{hh})$ is taken as the theoretical value at 52°, which is the last point plotted in the theoretical curve for σ_{hh}. From Figure 24a for C band, it seems that a substantial amount of noise or a very low SNR_0 would be necessary to reduce calculated values to measured data. Backscattering coefficients from multiyear ice is high compared with those from other ice types, and it is most likely that SNR_0 for multiyear ice is also high due to the higher returned signals. Thus the low magnitude of ρ for multiyear ice is only partially caused by noise, with higher order scattering responsible for the remaining difference. At L band, Figure 24b for multiyear ice suggests that noise effects, as well as multiple scattering, is smaller as compared with C band.

Results for first-year ice are presented in Figure 25, where $\mathrm{ref}(\sigma_{hh}) = \sigma_{hh}(\theta_{0i} = 52°)$. As seen in Figure 25a, the noise at C band for first-year ice can bring theoretical calculations down to the level of the measured data. Scatterer fractional volume in first-year ice is only 2.6%, which indicates that multiple scattering is not as important as in the case for multiyear ice, where scatterer fractional volume is 13%. At L band the theory underestimates the magnitude of ρ by a small amount as seen in Figure 25b, and thus noise will further bring down the calculated values. This supports the observation that the noise effect in L band is smaller than in C band.

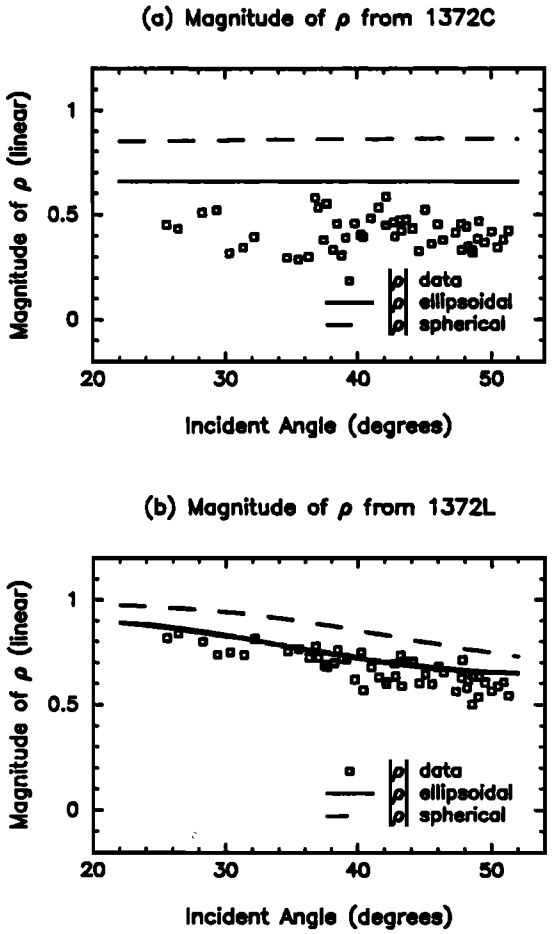

Figure 22. Comparisons of measured and calculated correlation coefficients for thin lead ice at (a) C band and (b) L band. Solid curves are calculated from the complete composite model with ellipsoidal brine inclusions. Dashed curves are for spherical brine inclusions.

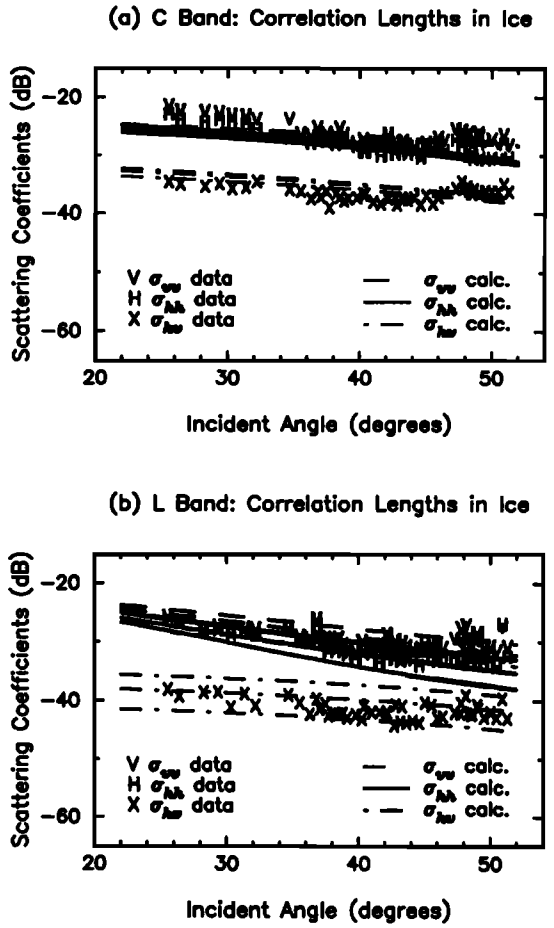

Figure 23. Variations in calculated coefficients due to ±25% change in correlation lengths of brine inclusions for (a) C band and (b) L band. For each type of backscattering coefficient, the upper curve is for the increase in correlation lengths, the lower is for the decrease, and the middle is the same as in Figure 18 or 19 replotted as a reference.

For thin ice, results shown in Figure 26 with $\mathrm{ref}(\sigma_{hh}) = \sigma_{hh}(\theta_{0i} = 52°)$, a signal-to-noise ratio less than that in first-year or multiyear ice is required to reduce the measured magnitude of ρ at C band frequencies to the observed values. This is the case, since backscattering coefficients from thin ice are small compared with those from other ice types. At L band the calculated magnitude of ρ is just a little higher than the measurement, and smaller noise can bring down the calculation to the measured level. In thin ice, scatterer fractional volume is 10%, and higher order scattering, which is more important at higher frequencies, can also cause more decorrelation between horizontal and vertical returns.

For polarimetric scattering coefficients used in this paper, the speckle effect is negligible, since covariance matrices are

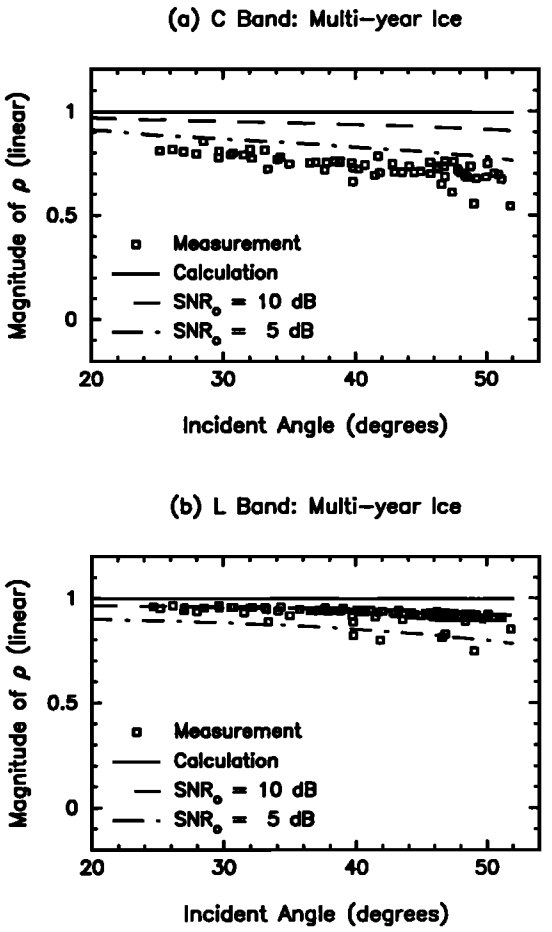

Figure 24. Effects of noise in correlation coefficient of multiyear ice at (a) *C* band and (b) *L* band.

ensemble averages over 1000 pixels. All data for sea ice, which are natural distributed targets, are at oblique incident angles; the data have zero mean and do not suffer from coherent contamination.

8. Summary and Discussion

In this paper, experimental observations of sea ice polarimetric signatures have been investigated with the composite model for different ice types, including multiyear, first-year, and thin lead ice. Fully polarimetric data were acquired by the multifrequency JPL SAR over the Beaufort Sea in March 1988 during the BSFC. ERS 1 SAR also supplies data at small incident angles for vertical polarization. Polarimetric data from six images for three sea ice scenes at *C* band and *L* band frequencies are analyzed. Sea ice characterization data collected by APLIS during BSFC and other field and laboratory experiments are utilized to relate sea ice polarimetric signatures to physical, structural, and electromagnetic properties of sea ice. Trends observed in polarimetric signatures of the ice types are explained by volume and surface scattering mechanisms in a layered anisotropic configuration under effects of various environmental conditions. Sensitivity studies of sea ice characterization parameters are carried out to investigate the corresponding variations in polarimetric signatures, and noise effects in signatures of the ice types are also considered.

At *C* band and *L* band frequencies, polarimetric signatures of multiyear sea ice show the isotropic characteristics of the medium structure. The signatures are dominated by the upper part of multiyear ice, which contains scatterers and surface features with less directional preference (such as randomly oriented air inclusions and composite roughness with azimuthally symmetric distribution). Volume composition of multiyear ice is responsible for the signatures at the middle range of incident angles. At small incident angles, hummocks and small-scale roughnesses are important to multiyear ice signatures, which have different behaviors at different wave frequencies. Hummocks also influence the signatures at large incident angles. Roughness at the snow-ice interface has stronger effects compared with the air-snow interface. Size variations of air inclusions in desalinated multiyear ice cause larger changes in *L* band signatures.

For first-year sea ice, temperature and salinity primarily determine the constituent phase distribution, which is important to wave propagation, attenuation, and polarimetric signatures. Crystallographic structure of columnar ice preferentially aligns brine inclusions and results in an effective anisotropy. This anisotropy decorrelates horizontal and vertical waves as seen in correlation coefficients between the two wave types. The anisotropic effect is reduced by snow cover containing randomly oriented ice grains. Orientation distributions of nonspherical scatterers are accounted for in

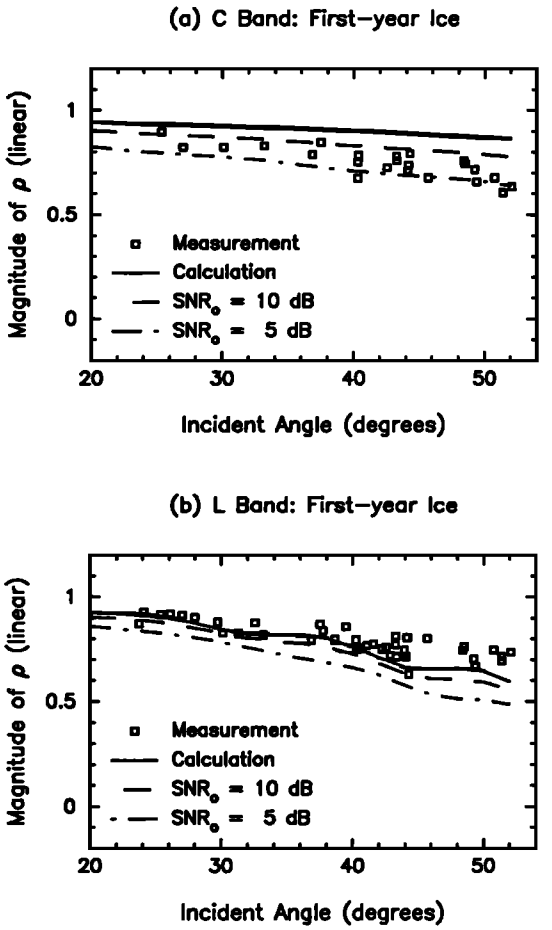

Figure 25. Effects of noise in correlation coefficient of first-year ice at (a) *C* band and (b) *L* band.

the model. Ellipsoidal shape of brine inclusions causes depolarization effects and is important to cross-polarized returns. For the measured surface parameters of the ice types under consideration, the decorrelation effect caused by rough surface are not dominant in polarimetric backscattering. Surface roughnesses at medium interfaces do not significantly affect signatures from inhomogeneities inside first-year ice at large incident angles. Brine inclusion size causes competing effects in wave attenuation and scattering and has opposing effects on signatures at the two different frequencies. Wave depolarization and decorrelation are both sensitive to axial ratios of characteristic lengths of brine inclusions.

Signatures of thin lead ice carry characteristics of volume and surface features of the ice layer under significant influence of a surface brine skim. Copolarized returns show a strong decreasing trend as functions of incident angles, and their ratio (γ) becomes large at large incident angles. However, cross-polarization ratios are large and decorrelation effects between horizontal and vertical waves are strong with small phase differences. The brine cover with a high permittivity reflects more wave energy at larger incident angles, reduces more horizontal wave transmission, and enhances copolarized ratio. The combination of volume and surface effects on wave interactions in thin ice gives rise to the decreasing behavior in magnitudes of copolarized correlation and scattering coefficients as seen in polarimetric signatures of thin ice at L band. Thus sea ice characteristics such as temperature, salinity, brine pockets, growth conditions, and surface composition are manifested in polarimetric signatures of thin ice.

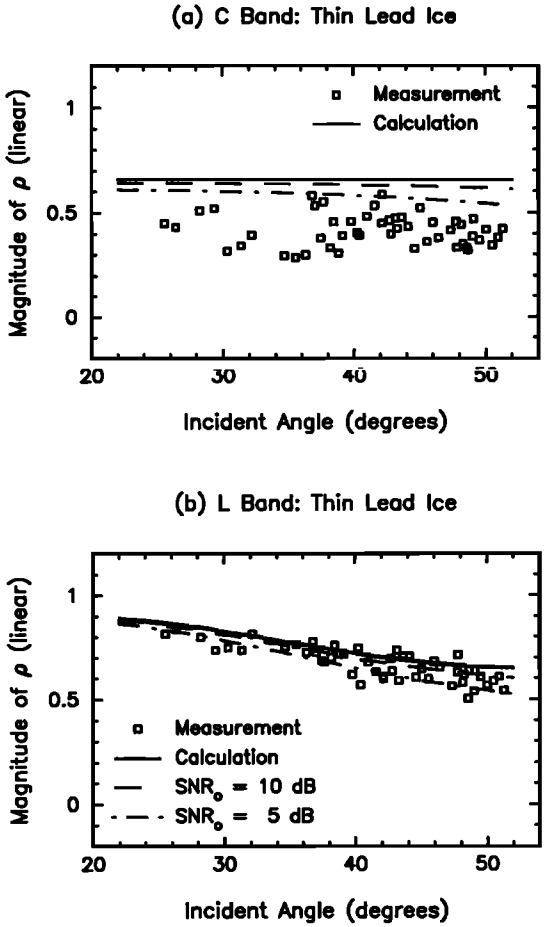

Figure 26. Effects of noise in correlation coefficient of thin lead ice at (a) C band and (b) L band.

Currently, the ERS 1 SAR is collecting σ_{vv} data for high-resolution radar mapping of sea ice and other geophysical zones [*Attema*, 1991]. The analysis in this paper helps identify major sources contributing to σ_{vv} of sea ice and thus provides an indication of the information contained in ERS 1 data. For identification and classification of ice types, results in this paper can be applied to select backscattering coefficients that are important to sea ice discrimination. Copolarized coefficients σ_{hh} or σ_{vv} of multiyear and first-year ice when used together with correlation coefficients improve the discrimination of the ice types at various incident angles. For example, compare the separation of ρ data in Figure 6b for multiyear ice and Figure 13b for first-year ice. The majority of data for multiyear ice in Figure 6b is in the range 0.9–1.0, while that for first-year ice in Figure 13b is in 0.6–0.9. These show a distinction between the ice types; note that all possible values or the entire dynamic range is between zero and 1 for the magnitude of ρ. Cross-polarized ratios provide further information pertaining to scattering mechanisms and structural properties of sea ice. Knowledge of ice thickness distribution, especially for young ice, is important to the prediction of heat transfer to the atmospheric boundary layer [*Maykut*, 1978]. To assess the possibility of ice thickness retrieval, the sea ice model relating polarimetric signatures to sea ice properties can be used to generate simulated data to study sensitivity, accuracy requirements, and noise effects in neural network or other inversion techniques.

For the first time, this paper series (Parts 1 and 2) comprehensively presents (1) calibrated multifrequency polarimetric signatures of sea ice from airborne radars in conjunction with spaceborne backscatter, (2) together with a collection of sea ice characterization parameters from many field and laboratory ice experiments, (3) in the context of a composite model that relates microwave signatures of several ice types to characteristics of sea ice. Various complex properties of sea ice have been included: the thermodynamic phase distribution of constituents in sea ice, orientation distribution of crystallographic c axes, nonspherical geometry of brine pockets and other inhomogeneities, anisotropy of columnar ice, thickness distribution in thin ice, brine layer and snow cover, roughnesses at sea ice interfaces, and melt hummocks.

The model provides physical insights into sea ice signatures observed by remote sensors in order to interpret the signature behavior and to assess the retrieval of important geophysical parameters of sea ice. Furthermore, the comparison of experimental data and theoretical results with parameters restricted by sea ice physics suggests directions for future experiments and improvements of state-of-the-art models. For instance, the present model needs to include higher order scattering for a better comparison of depolarization (σ_{hv}) and decorrelation (ρ) data at high frequencies. Various ice types, such as rafted ice, pressure ridges, composite pancakes, refrozen melt ponds, grease ice, and other ice types, are not addressed here. An important feature of thin new ice to be considered is frost flowers, which are clusters of ice crystals with a high salinity on the ice surface, giving rise to strong scattering. Further developments are

therefore necessary for more complicated physical and structural properties of sea ice under effects of environmental and seasonal conditions.

Acknowledgments. The authors thank D. K. Perovich for the description of brine skim on thin ice and A. Carlström for the surface roughness data. The research described in this paper was carried out by the Jet Propulsion Laboratory, California Institute of Technology, and was sponsored by the Office of Naval Research and the National Aeronautics and Space Administration.

References

Arcone, S. A., A. J. Gow, and S. G. McGrew, Structure and dielectric properties at 4.8 and 9.5 GHz of saline ice, *J. Geophys. Res.*, *91*(C12), 14,281–14,303, 1986.

Attema, E. P. W., The active microwave instrument on-board the ERS-1 satellite, *Proc. IEEE*, *79*(6), 850–866, 1991.

Carlström, A., Surface roughness measurements during Beaufort Sea Ice, 1, in *Field Data Report—Beaufort Sea Ice 1*, edited by L. D. Farmer, Bronson Hills Associates, Fairlee, Vermont, 1992.

Cavalieri, D. J., J. P. Crawford, M. R. Drinkwater, D. T. Eppler, L. D. Farmer, R. R. Jentz, and C. C. Wackman, Aircraft active and passive microwave validation of sea ice concentration from the Defense Meteorological Satellite Program special sensor microwave imager, *J. Geophys. Res.*, *96*(C12), 21,989–22,008, 1991.

CEAREX Drift Group, CEAREX drift experiment, *Eos Trans. AGU*, *71*(40), 1115, 1990.

Cox, G. F. N., and W. F. Weeks, Salinity variations in sea ice, *J. Glaciol.*, *13*(67), 109–120, 1974.

Cox, G. F. N., and W. F. Weeks, Equations for determining the gas and brine volumes in sea ice samples, *J. Glaciol.*, *29*(12), 306–316, 1983.

Drinkwater, M. R., Beaufort Sea 90 snow conditions, in *Field Data Report—Beaufort Sea Ice 1*, edited by L. D. Farmer, Bronson Hills Associates, Fairlee, Vermont, 1992.

Drinkwater, M. R., and G. B. Crocker, Modeling changes in the dielectric and scattering properties of young snow-covered sea ice at GHz frequencies, *J. Glaciol.*, *34*(118), 274–282, 1988.

Drinkwater, M. R., J. P. Crawford, D. J. Cavalieri, B. Holt, and F. D. Carsey, Comparison of active and passive microwave signatures of Arctic sea ice, *JPL Tech. Publ.*, *90-56*, 29–36, 1991a.

Drinkwater, M. R., R. Kwok, D. P. Winebrenner, and E. Rignot, Multifrequency polarimetric synthetic aperture radar observations of sea ice, *J. Geophys. Res.*, *96*(C11), 20,679–20,698, 1991b.

Evans, S., Dielectric properties of ice and snow—A review, *J. Glaciol.*, *5*, 773–792, 1965.

Gow, A. J., S. A. Arcone, and S. G. McGrew, Microwave and structure properties of saline ice, *Rep. 87-20*, U.S. Army Corps of Eng., Cold Reg. Res. and Eng. Lab., Hanover, N. H., 1987.

Gow, A. J., D. A. Meese, D. K. Perovich, and W. B. Tucker III, The anatomy of a freezing lead, *J. Geophys. Res.*, *95*(C10), 18,221–18,232, 1990.

Klein, L. A., and C. Swift, An improved model for the dielectric constant of seawater at microwave frequencies, *IEEE Trans. Antennas Propagat.*, *AP-25*(1), 104–111, 1977.

Kwok, R., and G. F. Cunningham, Backscatter characteristics of the winter ice cover in the Beaufort Sea, *J. Geophys. Res.*, *99*(C4), 7787–7802, 1994.

LeadEx Group, The LeadEx experiment, *Eos Trans. AGU*, *74*(35), 393, 1993.

Maykut, G. A., Energy exchange over young sea ice in the central Arctic, *J. Geophys. Res.*, *83*(C7), 3646–3658, 1978.

Meese, D. A., The chemical and structural properties of sea ice in the southern Beaufort Sea, *CRREL Rep. 89-25*, U.S. Army Corps of Eng., Cold Reg. Res. and Eng. Lab., Hanover, N. H., 1989.

Nghiem, S. V., S. H. Yueh, R. Kwok, and F. K. Li, Symmetry properties in polarimetric remote sensing, *Radio Sci.*, *27*(5), 693–711, 1992.

Nghiem, S. V., R. Kwok, S. H. Yueh, and M. R. Drinkwater, Polarimetric signatures of sea ice, 1, Theoretical model, *J. Geophys. Res.*, this issue.

Onstott, R. G., Polarimetric radar measurements of artificial sea ice during CRREL-EX'88, *Tech. Rep. 196100-23-T*, Environ. Res. Inst. of Mich., Ann Arbor, 1990.

Perovich, D. K., and J. A. Richter-Menge, Surface characteristics of lead ice, *J. Geophys. Res.*, *99*(C8), 16,341–16,350, 1994.

Sihvola, A. H., and J. A. Kong, Effective permittivity of dielectric mixtures, *IEEE Trans. Geosci. Remote Sens.*, *26*(4), 420–429, 1988.

Stogryn, A., and G. J. Desargant, The dielectric properties of brine in sea ice at microwave frequencies, *IEEE Trans. Antennas Propagat.*, *AP-33*(5), 523–532, 1985.

Thorndike, A. S., D. A. Rothrock, G. A. Maykut, and R. Colony, The thickness distribution of sea ice, *J. Geophys. Res.*, *80*(33), 4501–4513, 1975.

Tiuri, M. E., A. H. Sihvola, E. G. Nyfors, and M. T. Hallikainen, The complex dielectric constant of snow at microwave frequencies, *IEEE J. Ocean Eng.*, *OE-9*(5), 377–382, 1984.

Tsang, L., J. A. Kong, and R. T. Shin, *Theory of Microwave Remote Sensing*, John Wiley, New York, 1985.

Vant, M. R., R. O. Ramseier, and V. Makios, The complex-dielectric constant of sea ice at frequencies in the range 0.1–40 GHz, *J. Appl. Phys.*, *49*(3), 1264–1280, 1978.

Weeks, W. F., and S. F. Ackley, *The Growth, Structure, and Properties of Sea Ice*, *Monogr. Ser.*, vol. 82-1, U.S. Army Corps of Engineers, Cold Regions Research and Engineering Laboratory, Hanover, N. H., 1982.

Wen, T., W. J. Felton, J. C. Luby, W. L. J. Fox, and K. L. Kientz, Environmental measurements in the Beaufort Sea, spring 1988, *Tech. Rep. APL-UW TR 8822*, Appl. Phys. Lab., Univ. of Wash., Seattle, 1989.

Yueh, S. H., J. A. Kong, and R. T. Shin, Calibration of polarimetric radars using in-scene reflectors, chap. 9, edited by J. A. Kong, pp. 451–510, Elsevier, New York, 1990.

Yueh, S. H., S. V. Nghiem, and R. Kwok, External calibration of polarimetric radar images using distributed targets, *JPL Tech. Publ.*, *92-14*, 62–64, 1992.

Yueh, S. H., S. V. Nghiem, and R. Kwok, Symmetrization of cross-polarized responses in polarimetric radar images using reciprocity, *IEEE Trans. Geosci. Remote Sens.*, *31*(6), 1180–1185, 1993.

M. R. Drinkwater, R. Kwok, S. V. Nghiem, and S. H. Yueh, Jet Propulsion Laboratory, MS 300-235, California Institute of Technology, 4800 Oak Grove Drive, Pasadena, CA 91109. (e-mail: nghiem@malibu.jpl.nasa.gov)

(Received July 7, 1994; revised December 7, 1994;
accepted March 9, 1995.)